AQUIFER ZONATION BASED ON JOINT INVERSIONS

Published in *Geophysics*:

Doetsch, J., Linde, N., Coscia, I., Greenhalgh, S. A., and Green, A. G., 2010. Zonation for 3D aquifer characterization based on joint inversions of multimethod crosshole geophysical data, *Geophysics*, **75**, G53-G64.

ABSTRACT

Predictive groundwater modeling requires accurate information on aquifer characteristics. Geophysical imaging is a powerful tool for delineating aquifer properties at an appropriate scale and resolution, but it suffers from problems of ambiguity. One way to overcome such limitations is to adopt a simultaneous multitechnique inversion strategy. We have developed a methodology for aquifer characterization based on structural joint inversion of multiple geophysical data sets followed by clustering to form zones and subsequent inversion for zonal parameters. Joint inversions based on structural cross-gradient constraints require less restrictive assumptions than, say, applying predefined petrophysical relationships, and generally yield superior results. This approach has, for the first time, been applied to three geophysical data types in three dimensions. A classification scheme using maximum likelihood estimation is used to determine the parameters of a Gaussian mixture model that defines zonal geometries from the joint inversion tomograms. The resulting zones are used to estimate representative geophysical parameters of each zone, which are then used for field-scale petrophysical analysis. A synthetic study demonstrates how joint inversion of seismic and radar traveltimes and electrical resistance tomography (ERT) data greatly reduces misclassification of zones (down from 21.3% to 3.7%) and improves the accuracy of retrieved zonal parameters (from 1.8% to 0.3%) compared to individual inversions. We applied our scheme to a data set collected in northeastern Switzerland to delineate lithological subunits within a gravel aquifer. The inversion models resolve three principal sub-horizontal units along with some important 3-D heterogeneity. Petrophysical analysis of the zonal parameters indicates ~30% variation in porosity within the gravel aquifer and an increasing fraction of finer sediments with depth.

1.1 INTRODUCTION

Aquifer characterization is a prerequisite for predictive groundwater modeling. Traditionally, small-scale aquifer properties are derived from geological and hydrological investigations at a limited number of boreholes. These investigations may include simple lithological interpretations of drill chips/cuttings and laboratory determinations of physical properties (e.g., hydraulic conductivity) of retrieved cores. The sampling volume for such measurements is very limited, being restricted to the actual borehole positions. Furthermore, the assumption that laboratory-determined physical properties represent in-situ conditions may not be valid because of significant scaling effects, differences in confining pressure, strain, and fracturing, and a natural sampling bias towards intact specimens. Geophysical well logging overcomes some of these problems and extends the sampling distance up to a maximum of approximately 1 m from the borehole. Nevertheless, upscaling information derived from laboratory measurements and well logs to help construct fluid-flow and transport models of heterogeneous formations does not always lead to accurate predictions [*Scheibe and Chien*, 2003].

Hydrologists often perform in situ pumping tests, which together with certain assumptions about aquifer homogeneity and isotropy, enable the aquifer to be characterized on a much broader scale. This constitutes the other extreme end member solution to the spatial scaling problem.

An intermediate scaling approach involves constraining hydrological models using appropriate crosshole and/or surface geophysical data. Geophysical imaging is particularly useful (and complementary) because it interrogates a much greater volume of the aquifer than simple drilling and logging, provides almost continuous subsurface sampling, and is capable of delineating heterogeneity. For example, *Scheibe and Chien* [2003] produce accurate predictions of bromide breakthrough curves using a combination of crosshole radar tomograms and flow-meter and slug-test data, whereas traditional hydrological data alone yield poor predictions. The success of this approach is attributed to the large spatial coverage and 0.1 – 1 m resolution of the radar tomograms combined with a strong correlation between radar wavespeed and effective porosity. For such approaches to produce meaningful results, there must be a strong empirical relationship between the tomographic (geophysical) parameter and the hydrological properties [*Day-Lewis and Lane*, 2004; *Linde et al.*, 2006b]. Unfortunately, petrophysical relationships are often site-specific, such that they cannot be easily extrapolated to other locations or geologic conditions. Likewise, simplified theoretical relationships between geophysical parameters and hydrological properties have limited ranges of applicability and cannot always be directly applied to geophysical tomograms based on standard inversions [*Day-Lewis and Lane*, 2004].

Although tomograms obtained from a single geophysical data type may help to improve hydrological models, ambiguity often remains. The conventional way to reduce such nonuniqueness is to introduce external constraints, such as à priori geological information, smoothing, stochastic regularization, or inversion for a specific model type. An alternative approach for reducing model ambiguity is joint inversion of two or more different types of co-located geophysical data to produce a single integrated model. The power of this approach lies in the complementary nature of the data and models that can be exploited to constrain the range of plausible hydrological interpretations. Since different geophysical methods (e.g., seismic and radar transmission and electrical resistance tomography [ERT]) are sensitive to different physical properties of an aquifer, joint inversion is traditionally achieved by imposing petrophysical relationships; multiple models are linked during the inversion by petrophysical equations with known parameter values [e.g., *Tryggvason et al.*, 2002]. For example, since resistivity and dielectric permittivity both depend on porosity [e.g., *Pride*, 1994; *Revil et al.*, 1998; *Linde et al.*, 2006a], this style of joint inversion could directly yield porosity estimates. A drawback of such schemes is that general petrophysical models typically involve many parameters that are likely to vary spatially and are usually poorly known.

A less restrictive approach to joint inversion, presented independently by *Haber and Oldenburg* [1997] and *Zhang and Morgan* [1997], is to impose structural similarity between models during the inversion process without any explicit assumptions about petrophysical relationships, except that the geophysical parameters are assumed to vary at common locations. *Gallardo and Meju* [2003; 2004] developed this structural approach into a methodology for joint inversion by advocating that the gradients of a model could be used to quantify structures. They introduced the idea that the vector cross product of the gradients of two models should be forced to zero (implying similar directions of the gradient vectors) at each iterative step of a joint inversion. Changes in the two parameters at a given location must then be either zero, parallel, or anti-parallel. *Gallardo and Meju* [2003] applied this approach to field data and used the final models for visual zonation and interpretation. One key advantage of the structural approach to joint inversion is that scatter plots between different models provide less biased information about petrophysical parameters than those obtained using direct petrophysical approaches to joint inversion [*Tryggvason and Linde*, 2006]. Several researchers have further modified and applied the cross-gradients joint inversion approach [e.g., *Gallardo and Meju*, 2007; *Linde et al.*, 2008], and it has recently been applied to more than two data types [*Gallardo*, 2007] and to 3-D data sets [*Linde et al.*, 2006a; *Tryggvason and Linde*, 2006; *Fregoso and Gallardo*, 2009]. We extend here the methodology developed by *Linde et al.* [2006a] to three different types of 3-D data.

Rather than using inverted tomograms to delineate the detailed structure of an aquifer [e.g., *Hubbard et al.*, 1999], it is often useful to integrate the information to define zones on a scale significantly larger than the inherent resolution of each tomogram. This allows us to determine "effective" geophysical parameters that are only weakly affected by the original regularization constraints. The zones thus identified are assumed to have similar petrophysical characteristics [*Hyndman and Gorelick*, 1996; *Hyndman and Harris*, 1996; *Eppstein and Dougherty*, 1998] and hence are more useful in flow and transport modeling. Whereas applications of zonation and classification techniques are common in medical imaging and remote sensing, they are still in their infancy in geophysics [*Avseth et al.*, 2001; *Bedrosian et al.*, 2007]. In near-surface investigations, *Tronicke et al.* [2004] and *Paasche et al.* [2006] have applied K-means and fuzzy c-means clustering techniques to crosshole traveltime and attenuation tomograms. Neither method is well suited for zone identification and classification of strongly correlated parameters, which is a fundamental requirement when applied to structurally constrained joint inversions. By using maximum likelihood estimation to find the parameters of a Gaussian mixture model, our preferred clustering approach incorporates the covariance between the various parameters [*Dempster et al.*, 1977; *Mitchell*, 1997]. As a consequence, this approach is explicitly aimed at determining zones for which there are strong correlations between the various parameters (e.g., Figure 4 in *Gallardo and Meju* [2003]).

In this contribution, we begin by explaining our inversion and clustering techniques and introducing the field test site in northern Switzerland. We then determine zonal models based on parameters estimated from structurally constrained joint inversions of comparable synthetic and field data sets, each comprising three different types of 3-D geophysical data (crosshole seismic, radar, and ERT). By fixing the zone boundaries defined by the joint inversion and clustering algorithms and re-inverting the same three data sets for uniform zonal parameter values (i.e., seismic and radar wavespeed and electrical resistivity), the effective parameters of each zone are established. As a final step, we use the estimated zonal parameters for the field example to infer hydrologically relevant properties, such as formation factor and relative variations in the distributions of fine materials (silts and clays).

1.2 METHODOLOGY

In this section we describe the main components of our scheme (i.e., joint inversion, cluster analysis and zonation, and zonal inversion). Figure 2.1 shows a flow-chart of the entire process from raw field data and à priori information to the final petrophysical properties of the aquifer.

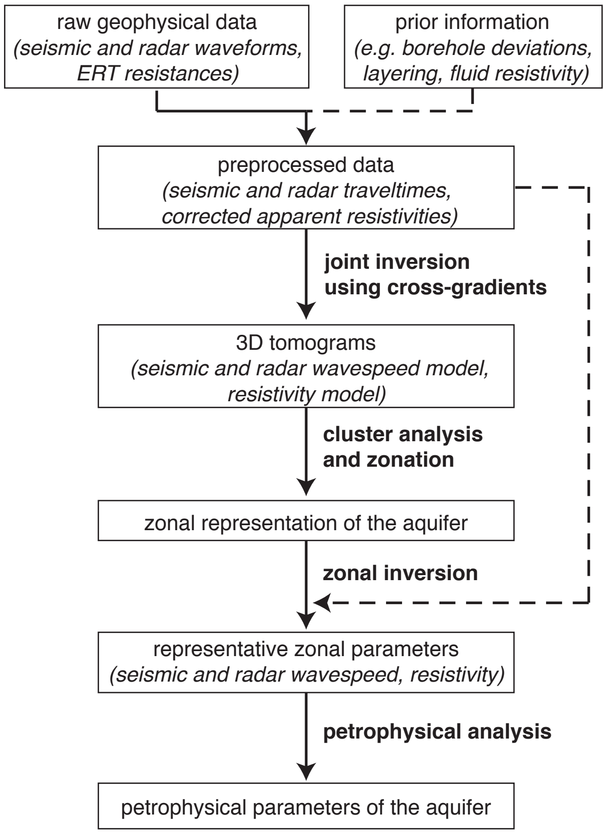

Figure 2.1. Workflow designed to locate aquifer zones and determine their petrophysical properties. Crosshole geophysical data - seismic, radar and ERT - are used as input to this scheme.

1.2.1 Joint inversion

Our formulation and implementation of the inverse problem is illustrated in Figure 2.2 and follows closely the scheme outlined by *Linde et al.* [2006a; 2008]. Forward solvers are used to calculate seismic and radar traveltimes, electrical resistances, and the corresponding sensitivities. The traveltimes and raypaths are calculated in the high frequency limit using a finite-difference algorithm [*Podvin and Lecomte*, 1991; *Tryggvason and Bergman*, 2006], and the electrical responses and related sensitivities are computed using a finite-element solver implemented by *Rücker et al.* [2006].

The objective function Φ for K different data sets is defined as

$$\Phi = \sum_{k=1}^{K} w_k (\Phi_{d(k)} + 10^{\varepsilon} \Phi_{m(k)}) + \lambda \sum_{k=1}^{K} \sum_{l<k} T_{kl} \tag{2.1}$$

with $\Phi_{d(k)}$ and $\Phi_{m(k)}$ being the data misfit and regularization term for data set k, and T_{kl} is the sum of the absolute values of the cross-gradient function $\mathbf{t}_{kl}$ between the models corresponding to data sets k and l (see below). The parameters w_k, ε and λ are the weighting factors for each data set, the regularization term, and the cross-gradients term, respectively.

When individually inverting a single data set, only $\Phi_{d(k)}$ and $\Phi_{m(k)}$ contribute to the objective function (Equation 2.1 and Figure 2.2): $\Phi_{d(k)}$ is the misfit between the observed data and the data predicted by the wavespeed or resistivity-models and $\Phi_{m(k)}$ quantifies the model regularization that penalizes model structure in some sense. We use a stochastic regularization operator (having weight 10^{ε} relative to the data fit term) based on an exponential geostatistical model that penalizes model complexity and deviations from the initial input model [*Linde et al.*, 2006a].

Joint inversion of two colocated data sets (e.g., radar and ERT) using a structural approach adds the third component to the objective function that enforces structural similarity [*Haber and Oldenburg*, 1997]. The structural similarity of two models $\mathbf{m}_k$ and $\mathbf{m}_l$ is quantified by calculating a normalized version of the cross-gradients function introduced by *Gallardo and Meju* [2003] at each location as [*Linde et al.*, 2008]

$$\mathbf{t}_{kl}(x,y,z) = \frac{\nabla \mathbf{m}_k(x,y,z) \times \nabla \mathbf{m}_l(x,y,z)}{\mathbf{m}_{k\_apriori}(x,y,z) \cdot \mathbf{m}_{l\_apriori}(x,y,z)} . \tag{2.2}$$

The normalization of Equation 2.2 is with respect to the à priori models $\mathbf{m}_{k\_apriori}$ and $\mathbf{m}_{l\_apriori}$. Note that the denominator never goes to zero. By normalizing the cross-gradients function, the constraints for each model combination have, for a given relative change in the model properties, the same weight in the optimization. The linearized normalized cross-gradients function of $\mathbf{m}_k$ and $\mathbf{m}_l$ is added as a constraint at each iterative step by giving it a large weight in the linear system of equations [*Linde et al.*, 2006a]. *Paige and Saunders* [1982] iterative conjugate gradient algorithm LSQR is used to minimize the objective function in a least-squares sense.

For three-method joint inversion, we calculate the cross-gradients function for every possible model combination to give three cross-gradients fields. These linearized cross-gradients constraints are imposed at each iterative step. *Gallardo* [2007] introduced an alternative approach that is based on the cross-product of a reference gradient (defined at each location as the strongest model gradient of all models in the previous iteration) and the gradients of each of the models being inverted for in the process.

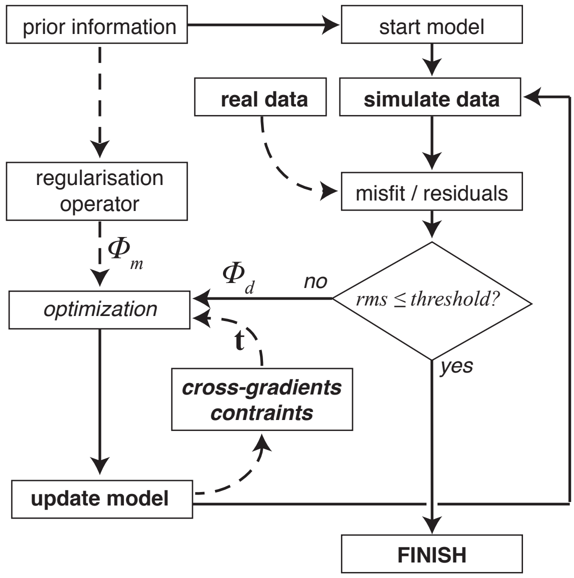

Figure 2.2. Flowchart of the joint inversion scheme using cross-gradients constraints. Φ_d and Φ_m represent the sole contributions to the objective function Φ (Equation 2.1) in individual inversions. For joint inversion, coupling between the models is introduced by penalizing deviations of the cross-gradient function **t** from zero during model optimization.

1.2.2 Zonation

We employ an unsupervised zonation algorithm to group model cells into zones distinguished by common physical characteristics, such that two or more zones with uniform properties are used to describe the distribution of geophysical parameters in a region of interest (e.g., an aquifer).

Defining the zones is a four-step process:

1. Preprocessing: The values of each input model (3-D tomogram) are scaled to a mean of 1 to avoid effects associated with the model units (e.g., km/s). The logarithm of electrical resistivity is used to compress the typically large range of values for this parameter. Classification needs reliable information from at least two methods for each cell and only model cells with ray coverage in either the seismic or radar forward models are used for the classification. This is guaranteed by sufficient ray coverage in one or both of the ray-based models plus the non-zero sensitivity of the ERT throughout the entire inversion domain. The decision of which cells to use for the cluster estimation could probably be improved by model appraisal (e.g., using the model covariance matrix) and might have to be adapted for surface-based data with generally coarser data coverage.

2. Cluster estimation: The clusters are modeled as a mixture of Gaussian functions with parameters that are automatically estimated on the basis of an expectation maximization

algorithm [*Bouman*, 1997]. This algorithm maximizes the probability of each cell belonging to a given set of clusters with optimized cluster parameters. The probability p_n that a cell n with model values $\mathbf{x}_n$ belongs to the k^{th} cluster is given by

$$p_n(k) = \frac{1}{(2\pi)^{M/2}} \left|\mathbf{R}_k\right|^{-1/2} \exp\left\{-\frac{1}{2}(\mathbf{x}_n - \mu_k)^t \mathbf{R}_k^{-1}(\mathbf{x}_n - \mu_k)\right\}, \tag{3}$$

where μ_k is the M - dimensional spectral mean and $\mathbf{R}_k$ is the covariance matrix of cluster *k*.

The cluster parameters are optimized as follows:

a) begin with a large number of clusters (e.g., 100);
b) classify all model cells and update statistics of the clusters;
c) combine the two statistically nearest neighbor clusters;
d) perform expectation maximization to update the mean and covariance of each cluster.

Steps b-d are repeated until a user-defined number of clusters is reached.

3. Classification: Each aquifer zone is represented by a single cluster and each cell is assigned to the zone for which $p_n(k)$ is maximal (Equation 2.3).

4. Zone interpolation: All poorly resolved cells not classified in step 3 are assigned to a zone based on interpolation/extrapolation of the well-resolved cells. The indicator kriging routine of the geostatistical software library GSLIB [*Deutsch and Journel*, 1998] is used for this purpose. The output of the indicator kriging is a zonal model of the entire model domain.

1.2.3 Zonal inversion

After obtaining a geometrical model of the zones, we perform an overdetermined inversion to find the optimum parameter values (i.e., the seismic and radar wavespeeds and electrical resistivity) of each zone. The zonal inversion uses the same forward operators and preprocessed data as used for the joint inversion (shown by the dashed arrow in Figure 2.1), but instead of inverting for many thousands of model parameters it only inverts for one parameter value of each geophysical method in each zone. Starting from a homogeneous initial model, a linearized iterative inversion scheme is used to optimize the zonal parameters. There is no need for additional regularization, because the inverse problem is strongly overdetermined (e.g., 5000 data points to define 3 parameters). The parameter update is slightly reduced at each iterative step to stabilize the non-linear inverse process.

Convergence of this inversion process is both fast and robust. The final data misfit can be used as an indicator of how well the zonal model can explain the geophysical data. If only a few model parameters in the zonal model can describe the data almost as well as relatively complex seismic, radar and ERT models with many thousands of parameters, then a zonal model is justified.

The inverted zonal parameters and any derived petrophysical properties are effective values on the scale of the zones, thereby providing a simple form of upscaling for use in future hydrological modeling. In most applications, it is highly unlikely that the underlying physical property distribution is made up of zones with uniform properties or overly smooth distributions. Constructing two end members of inversion models can help to understand the characteristics of the system under study.

1.3 FIELD SITE, PARAMETERS, AND PROCEDURES COMMON TO THE SYNTHETIC AND FIELD EXAMPLES

We have applied our methodology to a field site beside the Thur River in northern Switzerland, where the hydrological, ecological and biochemical effects of river restoration are currently being investigated [*RECORD*, 2011]. Our experiment is one component of a hydrogeophysical pilot study that targets a gravel aquifer in direct contact with an unrestored section of the river. We wish to estimate the spatial variability of geophysical and hydrogeological properties of the ancient river sediments forming the aquifer and to derive a 3-D zoned representation of the subsurface as a basis for future hydrogeophysical inverse modeling.

In this section we describe the following details that are common to the synthetic and field examples: geological/geophysical model, borehole geometry, recording configurations and processing parameters. The synthetic example helps to validate our new approach and guide the interpretation of the field data and associated models.

1.3.1 Experimental setup

Cores from boreholes across the field site reveal a laterally extensive three-layer structure with a 3-m-thick silty sand layer at the top, an intermediate-depth 7-m-thick gravel aquifer, and a thick impermeable clay aquitard at the base. The water table is normally at 4 m depth except during river flood events. For our experiment, the aquifer is accessed by four 11.4-cm-diameter fully-slotted PVC-cased boreholes located at the corners of a 5 × 5 m square, approximately 10 m from the river (Figure 2.3). Our analysis is concerned with this 5 × 5 m section of the 6-m-thick saturated part of the aquifer.

For the inversion of all three data sets, the area of interest is represented by a $7 \times 7 \times 6$ m volume containing a cubic mesh with 0.25 m edge lengths. The ERT model includes additional layers above and below this volume, but no regularization is applied across the boundaries to these layers. This is done because the boundaries are known to be sharp and because continuous regularization across these boundaries causes inversion artifacts within the gravel unit. A finer cubic mesh with 0.0625-m edge lengths is employed for the forward modeling of the seismic and radar traveltimes, whereas tetrahedra with 0.25-m edge lengths are used for the ERT forward modeling. Boundary effects in the ERT forward modeling were avoided by using a much larger domain than for the inversion and by using mixed type boundary conditions [*Rücker et al.*, 2006].

Crosshole seismic, radar, and ERT data were acquired across all six planes between the four boreholes. Seismic data were recorded using source and receiver spacings of 0.25 m, whereas radar data were collected with source and receiver spacings of 0.5 m and 0.1 m, respectively. To ensure full symmetric radar coverage, the source and receiver antennas were interchanged and the experiment repeated for each plane. For the ERT survey, 9 electrodes at 0.7-m intervals were deployed in each borehole. We used two different types of electrode configuration [*Bing and Greenhalgh*, 2000]: the AB-MN configuration with two current electrodes (A, B) in one borehole and two potential electrodes (M, N) in a second borehole, and the AM-BN configuration with one current and one potential electrode in a common borehole and the other two electrodes in a second borehole. Data using all possible combinations of bipole size and position were acquired in each plane, resulting in a total of 2464 AB-MN and 7776 AM-BN measurements. To speed up the inversions, the 10240 measurements were reduced to the 5000 most information-rich values using an experimental design procedure (for details see Chapter 4).

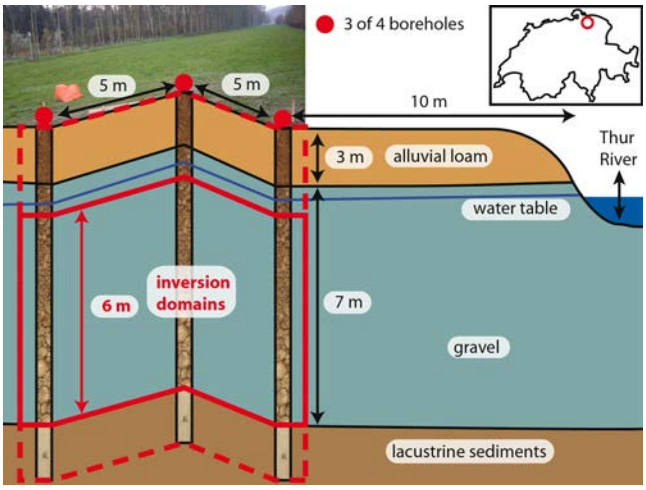

Figure 2.3. Cross section of the field site located close to the Thur River in northeastern Switzerland (see inset). The gravel aquifer is intersected by four boreholes located at the corners of a 5 m x 5 m square approximately 10 m from the river. Our inversion domain has horizontal dimensions of 7 m x 7 m for all data and a vertical extent of 6 m for the seismic and radar data (solid red rectangle) and 12 m for the ERT data (dashed red rectangle).

1.3.2 Inversion parameters

During inversion, stochastic regularization was used with an exponential model [*Deutsch and Journel*, 1998]. To honor the subsurface layering evident in the borehole cores, without imposing excessive constraints, we used 1.5- and 0.75-m integral scales in the horizontal and vertical directions, respectively. Because no detailed geostatistical analysis had been carried out at this site, the integral scales were chosen in a pragmatic manner to be comparable to the resolving capabilities of the geophysical data but smaller than the borehole spacing. The integral scales were varied about the chosen values without significant changes in the final inversion results. The same geostatistical model was used for the indicator kriging.

Initial homogeneous input models were seismic wavespeed α = 2.05 / 2.05 km/s, radar wavespeed v_r = 76 / 76 m/µs and electrical resistivity ρ = 250 / 180 Ωm for the synthetic / field examples. The standard deviation of the stochastic regularization was 10% of the input models for the seismic and radar experiments, corresponding to the expected variations in the field example and the variations used in the synthetic model. The ERT data were inverted for the logarithm of the resistivity, assuming a 20% standard deviation for the stochastic regularization.

Strong regularization (high ε, see Equation 2.1) was employed for the initial inversion step and then progressively decreased with a specified step length after each iteration until the normalized root mean squared (RMS) misfit reached a predefined threshold (see Figure 2.2).

Successively decreasing ε stabilizes the linearized inversion compared to using the final ε throughout the inversion process. To compare the results between individual and joint inversion as well as between the different methods, the target normalized RMS misfit was set to a uniform 1.2. It was possible to invert for a normalized RMS misfit of 1.0, corresponding to the actual error level in the synthetic example, but this led to inversion artifacts that adversely affected the subsequent cluster classification.

All inversions reached the target misfit after 10-19 iterations. Convergence could be achieved with fewer iterations by decreasing ε at a higher rate, but this resulted in higher values of the cross-gradients function in the final model [see *Linde et al.*, 2008]. The value of the ε was the same for all data sets during joint inversion, but each data set was weighted differently in the objective function and when calculating the model updates. The data set weights w_1 - w_3 were applied to the data misfit and the regularization of the corresponding model (Equation 2.1). They were initialized to compensate for the different number of measurements in each data set (in inverse proportion) and varied until the 3-D tomograms of all methods predicted the data equally well. Figure 2.4 illustrates the process we used to determine w_1 - w_3 and Table 2.1 shows the final inversion parameters for the synthetic and field examples. Tests using all possible combinations of two-method joint inversions and varying the inversion parameters gave very similar results to what is presented below for the three-method joint inversion, thus demonstrating the robustness of the methodology and each sequential part of it.

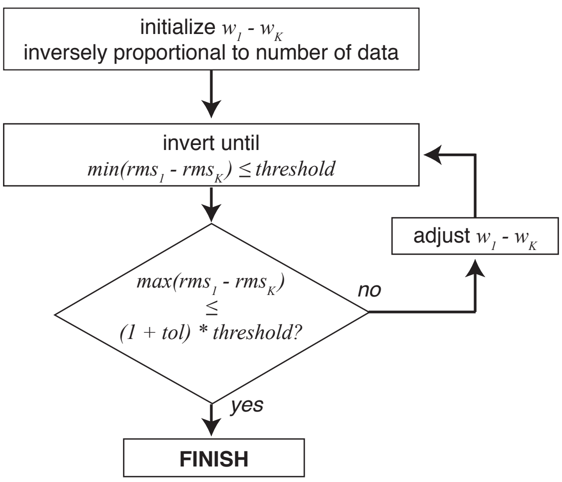

Figure 2.4. Flow chart of the procedure to determine the relative weights w_1 - w_K of the K different data sets for joint inversion. The threshold of the normalized RMS was set to 1.2 and the tolerance between the methods was chosen as tol = 0.04.

Table 2.1. Inversion parameters for the synthetic and field examples. In the column and row headers: *S* - seismic; *R* - radar; *E* - ERT individual inversions; *SRE* - joint inversion of all three methods.

Data set	geophys. method	weight w_k			ε	iterations	RMS misfit			
		S	*R*	*E*			*S*	*R*	*E*	mean
synthetic example	*S*	1			1.10	10	1.19			1.19
	R		1		1.20	10		1.18		1.18
	E			1	1.08	10			1.20	1.20
	SRE	1.3	1.0	1.0	0.98	16	1.17	1.17	1.20	1.18
field example	*S*	1			1.15	10	1.20			1.20
	R		1		1.20	10		1.21		1.21
	E			1	1.12	10			1.21	1.21
	SRE	1.5	1.2	1.0	0.88	19	1.20	1.16	1.20	1.19

1.4 SYNTHETIC EXAMPLE

The synthetic input model (Figure 2.5) was chosen to mimic the field situation. It consists of three sub-horizontal layers, of which the middle layer has the highest seismic and radar wavespeeds and resistivity. Its thickness varies from 2.5 m in one corner to 1 m in the opposite corner. The seismic wavespeed α and resistivity ρ are lowest in the bottom layer, whereas the radar wavespeed v_r is lowest in the top layer. For the ERT modeling, an additional top layer with a resistivity of $\rho = 1000\,\Omega\text{m}$ representing the unsaturated zone, and a bottom layer with a resistivity of $\rho = 25\,\Omega\text{m}$ representing the clay aquitard, are added.

Source, receiver, and electrode positions, as well as the measuring configurations were identical to the field example. The synthetic data were created with the same forward solvers and grid as used for the inversions. The 2661 seismic and 5584 radar traveltimes were contaminated with 1% and the 5000 apparent resistivities with 3% uncorrelated Gaussian noise prior to inversion.

1.4.1 Individual and joint inversion results

The three data sets are inverted separately and jointly. All resulting 3-D tomograms (Figure 2.6) recover the main features of the synthetic input models (Figure 2.5), albeit with somewhat gradual rather than abrupt transitions between the layers. The seismic and radar models obtained by individual inversion (Figure 2.6a and b) clearly resolve the high wavespeed center region. Low wavespeed parts are less well resolved, especially for the radar model. This is mainly due to the limited ray coverage, particularly crossing rays, in the top and bottom regions of the model. The individual ERT inversion (Figure 2.6c) resolves the two low resistivity zones, but the high resistivity layer in the middle is not continuous, as it should be. This poor performance in the center is attributed to current channeling in the high conductivity zones above and below and to the much higher sensitivities around the electrodes.

The 3-D seismic and radar tomograms resulting from joint inversion (Figure 2.6d and e) are very similar to the individual inversion tomograms, but the values of the low wavespeed regions are closer to the true values. The improvement in the joint inversion ERT tomogram (Figure 2.6f) is more pronounced, because the radar and seismic data help to constrain the geometry of the more resistive middle layer. Despite the restriction of rays to the acquisition planes and the concentration of ERT sensitivities around the boreholes, the homogeneous layers are well retrieved in 3-D, including the regions between the acquisition planes. The values of the cross-gradients function between the models were decreased by more than a factor of 100 compared to the individual inversions.

An informative view of the difference between models obtained from the individual and joint inversions is supplied by the scatter plots of Figure 2.7a-c and e-g. Whereas the scatter plots derived from the individual inversion show no evidence of clustering (Figure 2.7a-c), those from the joint inversion are sharply defined and relatively easy to classify (Figure 2.7e-g).

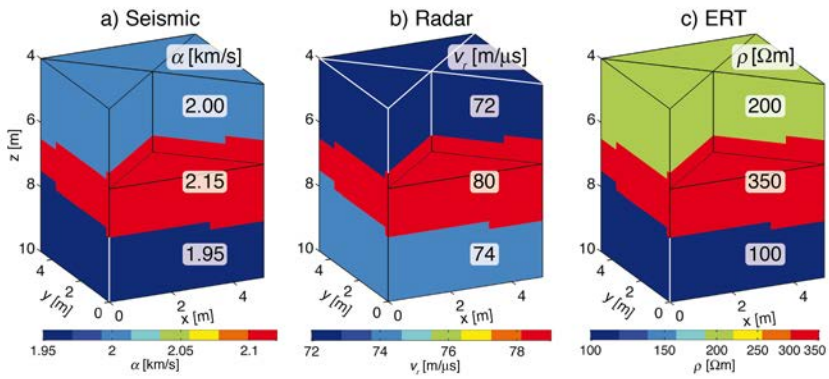

Figure 2.5. Input model used to create the synthetic data. It consists of three layers, the middle one of which has high seismic and radar wavespeeds α and v_r and a high resistivity ρ relative to the others. The thickness of this middle layer varies between 1 and 2.5 m at opposite corners. The synthetic data were contaminated with Gaussian noise (1% for seismic and radar traveltimes, 3% for apparent resistivities) before inversion. The boreholes used for the measurements are located at the four corners of the input model.

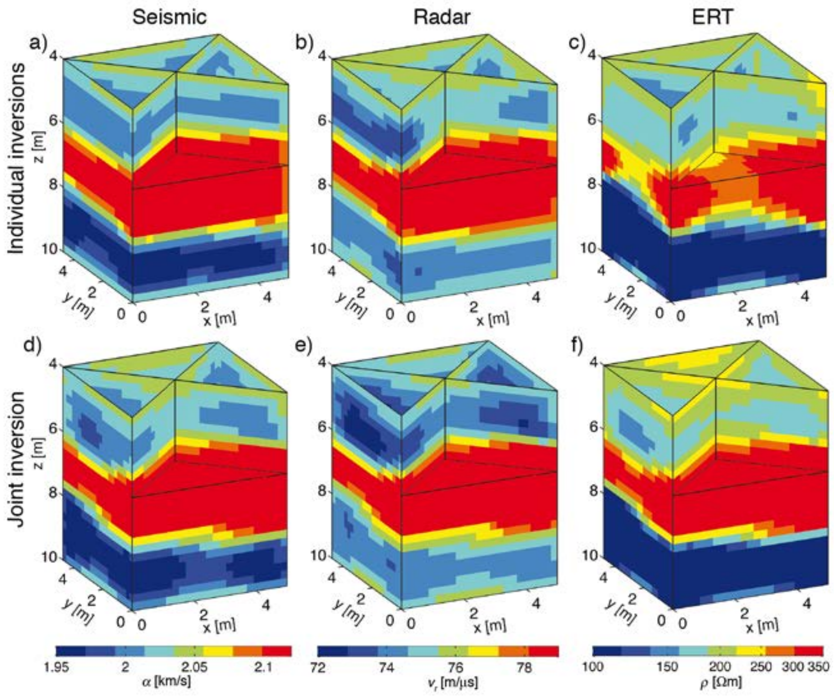

Figure 2.6. Results of (a-c) individual and (d-f) joint inversions of the synthetic data sets. All models fit the data with a normalized RMS misfit of 1.2 (1.0 corresponds to the error level). The main layering of the input model (see Figure 3) is observed in all models. The two seismic (a and d) and two radar (b and e) models are very similar, but a clear improvement is observed in the ERT model obtained by joint inversion (f) compared to the individual inversion model (c).

1.4.2 Classification

The scatter plots are now used for cluster estimation and zonation. The final number of zones was set to the true value of three for the synthetic study. Differences in the scatter plots are reflected in the classifications. The 50% confidence ellipsoids for each cluster are much smaller and more needle-like for the joint inversion (Figure 2.7h) than for the individual inversion results (Figure 2.7d). Outputs of the classification algorithm are the zonal models shown in Figure 2.8. The zonation based on the joint inversion tomograms (Figure 2.8c) is a much better reconstruction of the input model (Figure 2.8a) than that based on the individual inversion models (Figure 2.8b). Misclassification is only 3.7% for Figure 2.8c compared with 21.3% for Figure 2.8b. It is remarkable that the zones defined from the joint inversion tomograms are geometrically continuous, even though the positions of the cells are not considered during classification.

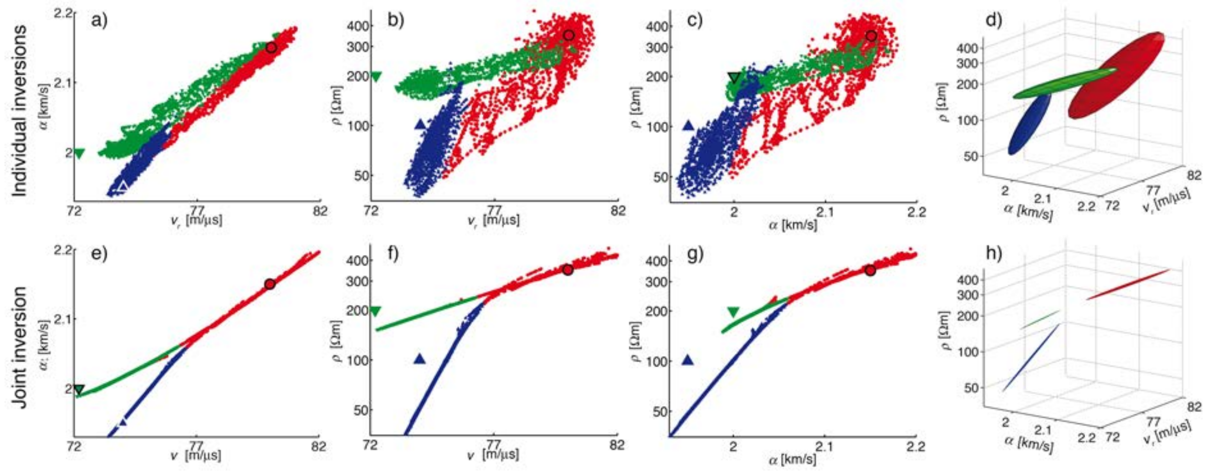

Figure 2.7. Scatter plots for the models obtained by (a-c) individual and (e-g) joint inversion together with visualizations of the automatically determined clusters used for zonation of the models obtained by (d) individual and (h) joint inversion. The larger triangles and circles in (a-c) and (e-g) show the true parameter values of each zone in the input model. The colors of the symbols in the scatter plots and cluster representation correspond to the respective zonal model in Figure 2.8.

1.4.3 Zonal inversion

The inverted zonal parameters and RMS misfits are shown at the base of Figure 2.8. The parameter values for each zone are much better retrieved through zonal inversion than by averaging the models in Figure 2.6 for each zone. The zonal model from joint inversion predicts the data with similar RMS misfits as for the 3-D tomograms (1.1-1.5), but the zonal model from individual inversions fails to do so (RMS misfits of 1.6-3.0).

The inverted zonal parameters reproduce the true values with a deviation of only 0.3% when using the zones derived from the joint inversion tomograms, whereas the deviation is 1.8% when using the zones derived from the individual inversion tomograms. A deviation of almost 2% in the parameter estimation is quite significant when compared to the 10-20% variation in the parameters of the synthetic input models (Figure 2.5).

The misclassification rates and matches of the geometry and parameter values (see images and tables in Figure 2.8) for the synthetic study demonstrate the superior performance of the joint inversion scheme vis-à-vis the individual inversion approach. For field data with unknown zone geometries and parameters, the zonation has to be judged on the basis of the RMS data misfit and by visual inspection. The performance of the method applied to field data is investigated in the next section.

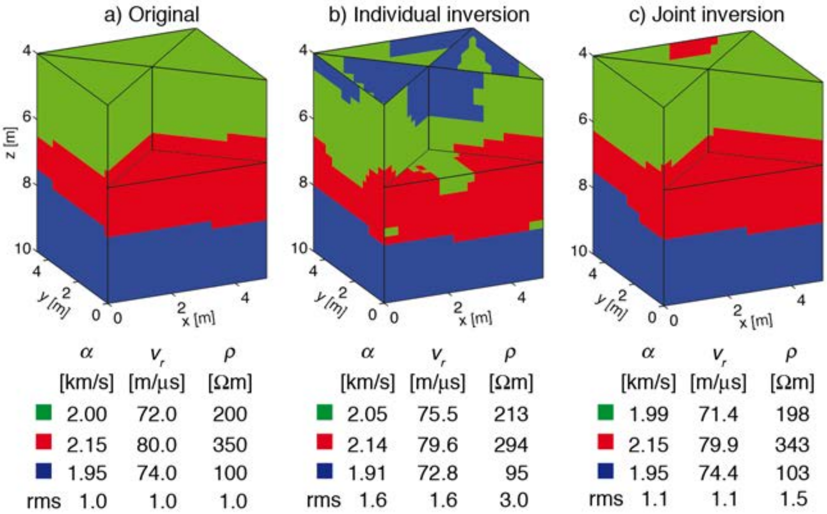

Figure 2.8. The (a) true zonal model (see Figure 5) and those derived by (b) individually and (c) jointly inverting the synthetic data. The zonal models derived from the individual and joint inversions have misclassification rates of 21.3% and 3.7%, respectively.

1.5 FIELD EXAMPLE

1.5.1 Measurements

Our field data were acquired with state-of-the art equipment. A sparker source was used to generate seismic waves with a center frequency of about 1 kHz, and hydrophones and a GEODE system were used to record the seismic data at a sampling rate of 21 μs. Very strong signals caused the seismic waveforms to be clipped, but the first arrivals could clearly be identified (e.g., Figure 2.9a). Crosshole radar data at a 0.4 ns sampling rate were acquired using a RAMAC 250 MHz system, which at our site had a center frequency of ~100 MHz with energy in the 50-170 MHz frequency range (e.g., Figure 2.9b). ERT resistances were recorded using a Syscal Pro resistivity meter. Borehole deviations were measured with a deviation probe using a three-axis fluxgate magnetometer for bearing and a three-axis accelerometer for inclination. Corrections for the borehole deviations were critical for the traveltime inversions.

Preprocessing of the seismic and radar data included manual traveltime picking and assignment of the correct source-receiver positions in the deviated boreholes. A total of 2661 seismic and 5584 radar traveltimes could be reliably picked. Seismic traveltimes ranged between 2.2 and 4.3 ms and radar traveltimes ranged between 60 and 116 ns, with estimated picking errors for both data sets of ~1%.

The ERT data were strongly influenced by the resistivity contrast between the borehole fluid and the formation, such that correction factors derived from modeling with and without the boreholes had to be applied (for details see Chapter 4). A 2.5% error in the apparent resistivity data was assumed in the subsequent inversions. A frequency polygon plot of apparent resistivities before and after application of the borehole-fluid corrections is displayed in Figure 2.9c.

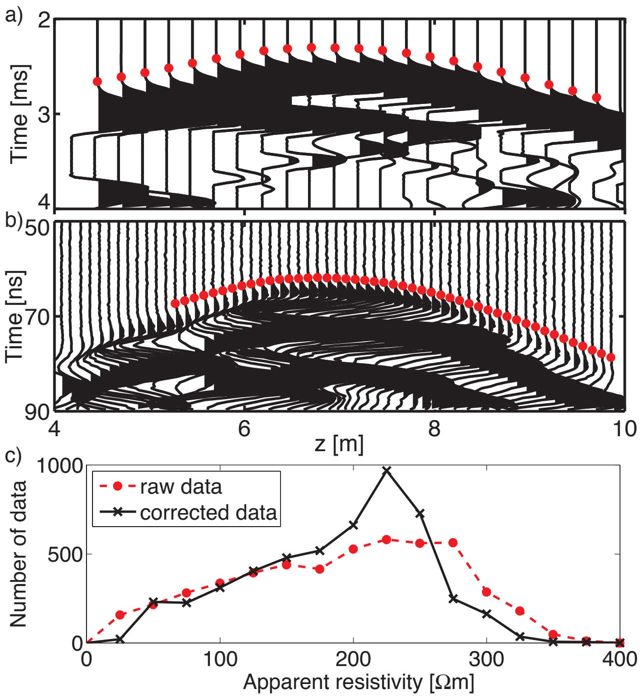

Figure 2.9. Typical raw (a) seismic and (b) radar source gathers for a source depth of 6.75 m. Red dots in (a) and (b) represent calculated forward responses of the final models obtained by joint inversion (see Figure 2.10d and e). (a) Although the seismic data were clipped, first arrivals could be reliably picked. (b) Picked first arrivals in the radar data do not include refracted waves through the unsaturated high wavespeed layer above 4 m; for the displayed source gather this means neglecting data collected above 5 m depth. (c) Frequency-polygon (histogram) of apparent resistivities plotted for raw and borehole-effect-corrected data.

1.5.2 Individual and joint inversion results

The models for the three parameter types obtained from the individual inversions contain very similar features, the most prominent being the high wavespeed and high resistivity layer in the middle of the domain (Figures 2.10a-c and 2.11a-c). Correlations between the models are relatively high (correlation coefficients > 0.6), even though each inversion is fully independent. This strong correlation indicates that all three methods sense the same geological/hydrological units, thus justifying the application of joint inversion to these data sets.

Seismic and radar tomograms from the three-method joint inversion (Figures 2.10d-e and 2.11de) are very similar to the individually inverted ones (Figures 2.10a-b and 2.11a-b), whereas resistivities in the jointly inverted ERT tomogram (Figures 2.10f and 2.11f) are noticeably more continuous than in the individually inverted one (Figures 2.10c and 2.11c). In similar fashion to the synthetic case, the magnitude of the cross-gradients between the models were reduced by more than a factor of 100 compared to the individual inversions. Although the images in Figure 2.10 are layered, when viewed from different directions (e.g., Figure 2.11) some pronounced 3-D heterogeneity is apparent. This heterogeneity is evident in all individual inversion tomograms (see Figure 2.11a-c), even though the sensitivity patterns of the traveltime and ERT data are fundamentally different with respect to location relative to the borehole.

The field example scatter plots in Figure 2.12 reveal the same variations between individual and joint inversion results as seen in the synthetic example (Figure 2.7). Although the scatter plots in Figure 2.12a-c show a general positive correlation between the geophysical parameters, the evidence for clusters is weak. By contrast, the joint inversion scatter plots in Figure 2.12e-g reveal distinct linear features.

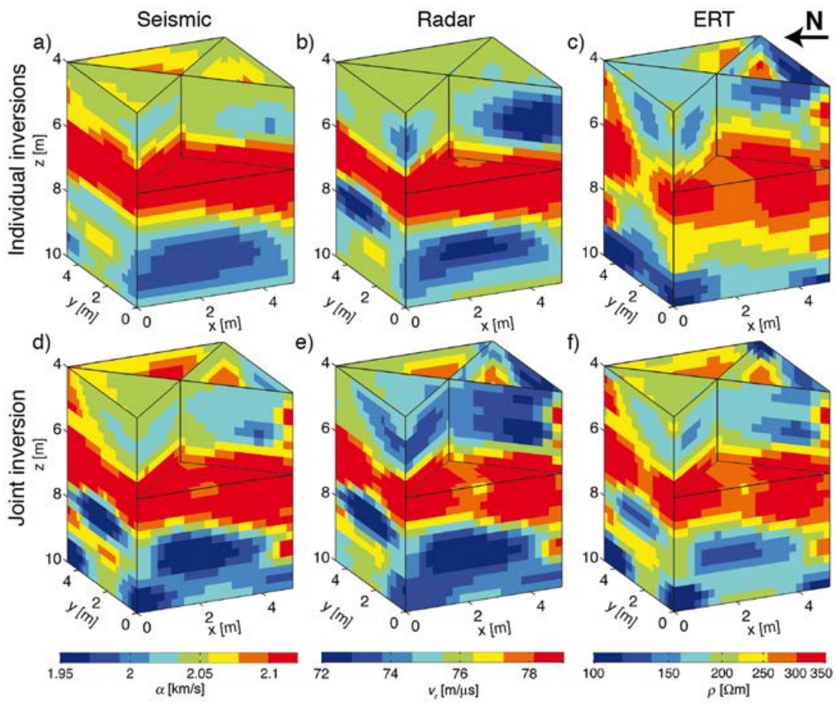

Figure 2.10. Results of (a-c) individual and (d-f) joint inversions of the field data set. All models fit the data with a normalized RMS misfit of 1.2 (1.0 corresponds to the error level). Note how the middle layer in the resistivity model obtained by joint inversion is more continuous than for the individual inversion.

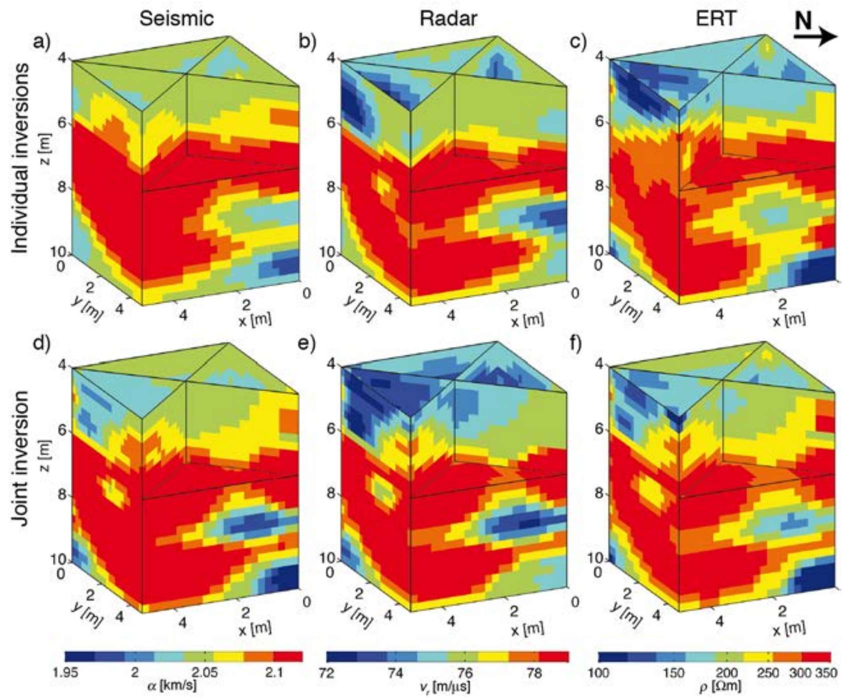

Figure 2.11. As for Figure 10, but viewed from a different direction. There are clear 3D structures and the individual inversions (a-c) show that all main features are detected independently by the three methods.

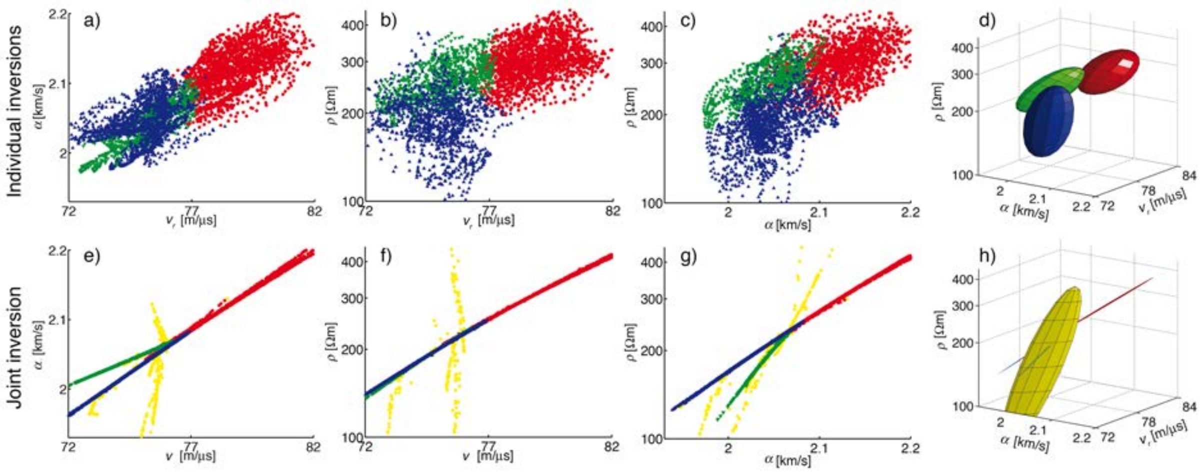

Figure 2.12. Scatter plots for the models obtained by (a-c) individual and (e-g) joint inversion together with visualizations of the automatically determined clusters used for zonation of the models obtained by (d) individual and (h) joint inversion. The scatter plots obtained from the individual inversion models are rather diffuse. They demonstrate a generally positive correlation between the geophysical parameters. In contrast, the scatter plots from the joint inversion models show well-defined linear correlations. (d) and (h) The different character of the scatter plots is also observed in the cluster visualizations. The large yellow cluster in (h) "collects" all of the poorly defined scatter points. These cells are reclassified by geostatistical interpolation (indicator kriging).

1.5.3 Classification and zonal inversion

Application of the classification algorithm to the scatter plots in Figure 2.12a-c and subsequent zonal inversion yields a high wavespeed and high resistivity zone in the center of the aquifer, but it cannot distinguish the regions at the top and bottom of this zone from each other (Figure 2.13a and d). Increasing the number of clusters does not improve this result.

To achieve the most meaningful classification of the scatter plots in Figure 2.12e-g, the results for different numbers of clusters were compared. We obtained the best result using four clusters, three of which are meaningful. The fourth is a “collector” cluster (yellow region in Figure 2.13b and e) in which most poorly resolved cells are placed. These poorly resolved cells are mostly found along the top or bottom of the inversion domain. Rather than leave gaps in these regions, we interpolate/extrapolate values from adjacent areas using the indicator kriging method. The resulting three zones in Figure 2.13c and f (referred to as model 1) are overall spatially aligned and this model is used in the subsequent interpretation.

The RMS misfits that result from the zonal inversion (see tables at the base of Figure 2.13) are very similar for all zoned models; the relatively low 1.4-1.5 misfit for the seismic and radar wavespeeds and 2.8 - 3.5 for the ERT resistivities is largely controlled by the common definition of the high wavespeed/resistivity zone in the center. Separating the top and the bottom layer does not significantly improve the misfit, even though the v_r and ρ values vary between these layers. The low RMS misfit for the ray-based methods indicates that a zoned wavespeed model is reasonable, whereas the higher RMS misfit for the ERT values indicates that smaller scale resistivity variations are necessary to fit the data adequately.

1.6 HYDROGEOPHYSICAL INTERPRETATION

1.6.1 Petrophysical analysis

The radar and resistivity values of model 1 (Figure 2.13c and f) for each zone (see table at the base of Figure 2.13f) are used as input to our petrophysical analysis along with the following parameters: (i) the resistivity of the pore water $\rho_w = 27$ Ωm (established from measurements in a nearby borehole at the time of the survey), (ii) the relative permittivity of the matrix κ_s, which we cannot determine exactly but is unlikely to have strong variations within the gravel aquifer (see later), and (iii) the cementation factor m which we take to be 1.5-1.6 [*Lesmes and Friedman*, 2005].

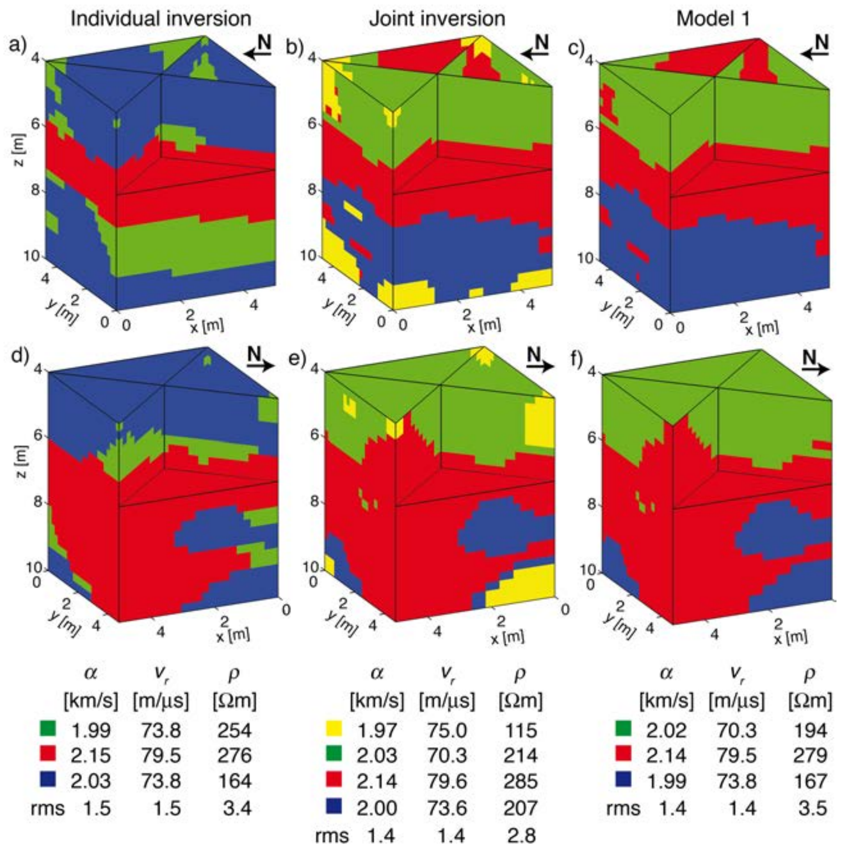

Figure 2.13. Zonal models based on the (a and d) individual and (b and e) joint inversions shown in Figures 2.10 and 2.11 viewed from two different directions. The final zonation based on the models obtained by joint inversion (model 1) in (c) and (f) is described in the text.

Seismic wavespeed is not explicitly included in the analysis. In unconsolidated environments, both seismic and radar wavespeeds are a function of porosity, but porosity estimates from seismic wavespeed are not as well constrained as those from radar wavespeed. Comparison of the seismic and radar wavespeeds with the Hashin-Shtrikman bounds [*Hashin and Shtrikman*, 1963] indicates a very well connected pore space [*Linde and Doetsch*, 2010] and thus motivates our choice of a relatively low cementation factor.

We use the petrophysical model of *Pride* [1994] to relate the relative permittivity

$$\kappa = \frac{c^2}{v_r^2} \;\; (c = 300 \text{ m/µs}) \tag{2.4}$$

to the formation factor F and porosity ϕ, linked by

$$F = \phi^{-m}. \tag{2.5}$$

in the following way:

$$\kappa = \frac{1}{F}\left[\kappa_w + (F-1)\kappa_s\right]. \tag{2.6}$$

Here $\kappa_w = 84$ is the relative permittivity of water at 10°C [*Eisenberg and Kauzmann*, 1969] and κ_s is the relative permittivity of the solid matrix. In the presence of fine-grain sediments (e.g., clays and silts), the electrical resistivity ρ can be related to F through a modified form of Archie's law [*Linde et al.*, 2006a]

$$\frac{1}{\rho} = \frac{1}{F}\left[\frac{1}{\rho_w} + (F-1)\sigma_s\right], \tag{2.7}$$

where σ_s is surface conductivity. Surface conductivity occurs as a result of the electrical triple layer that forms at the interface between grains that comprise the sediment matrix and water. It is most prominent in materials with large specific surface areas such as clays and silts [e.g., *Revil et al.*, 1998].

We solve Equation 2.6 for F (and ϕ using Equation 2.5) and then use Equation 2.7 to estimate σ_s. To estimate F and ϕ we have to assume a value for κ_s. We use $\kappa_s = 8.0$ to force surface conductivity $\sigma_s > 0$ in all three zones. The value of κ_s is not established at this site, although it is known to lie within a restricted range for the lithologies under consideration. It is also reasonable to assume that variations of κ_s within the gravel aquifer are likely to be quite small. Whatever value is used should not affect the relative variations in the deduced petrophysical parameters, but absolute values should be interpreted with caution. The range for ϕ in Table 2.2 corresponds to the likely variation in cementation factor *m*.

1.6.2 Interpretation

Two main findings result from this analysis (Table 2.2): (i) there is a distinct increase in surface conductivity σ_s with depth and (ii) porosity ϕ is significantly lower in the middle layer. The bottom layer was found to have a total average conductivity of 6 mS/m (167 Ωm), of which surface conductivity σ_s is predicted to contribute about one third (2.1 mS/m). The increase in σ_s can be attributed to a higher clay/silt fraction, demonstrating that it cannot be neglected in this sedimentary setting. Application of the conventional Archie's law [*Archie*, 1942] to the resistivity values for the bottom layer would overestimate ϕ by 25%.

A ~30% variation of ϕ between the middle and the top and bottom layers is quite well resolved. Small scale variations are expected to be even larger. In contrast, the differences between ϕ in the top and bottom layers are not very well defined. For example, the differences in radar wavespeed can be explained by variations in the cementation factor (see Table 2.2). This possibility is supported by the very small differences in seismic wavespeed between the upper and lower zones, which imply similar porosities assuming that there are no major differences in lithology [e.g., *Carcione et al.*, 2007].

Although porosity is not well defined by our data and analysis, the more relevant parameters as far as fluid transport is concerned are the well-constrained formation factor F and surface conductivity σ_s [e.g., *Revil and Cathles*, 1999]. The hydrological implications of our results are being investigated with ongoing time-lapse ERT measurements.

Table 2.2. Result of the petrophysical analysis.

Layer	F	σ_s [mS/m]	ϕ [%]
Top (green)	7	0.2	26 - 29
Center (red)	12	0.6	19 - 21
Bottom (blue)	9	2.1	23 - 26

1.7 DISCUSSION

The tomographic models from the joint inversion and the corresponding zonal models are complementary representations of the situation at our field site. Models obtained from joint inversion display small-scale variability, but these variations are strongly affected by the regularization applied. As a consequence, they cannot be used directly to determine quantitative petrophysical values from theoretical models such as those described by Equations 2.6 and 2.7 [*Day-Lewis and Lane*, 2004]. By comparison, the zonal inversion based on structures determined from clustering the joint inversion results yields physical parameters (e.g., seismic wavespeed) for relatively large zones. Such effective parameters are suitable for petrophysical analysis at field scales, but because small-scale variability is neglected the results are only meaningful if large-scale zones dominate the physical property fields.

The data misfit of the zonal parameter estimates is a measure of confidence in the zonal representation. For our field example, this implies that there are only minor seismic and radar wavespeed variations within the zones, because the zonal models can fit the data relatively well with a normalized RMS misfit of 1.4. In contrast, additional small-scale variability or vertical trends are probably needed to improve the fit to the ERT data (RMS misfit is a comparatively poor 3.5 for the zonal inversion values). This high misfit can also partly be caused by small errors in the assumed location of the water table and the clay aquitard, because no electrodes were located outside the saturated gravel.

1.8 CONCLUSIONS

We have presented a methodology for hydrogeophysical aquifer characterization based on cross-gradients joint inversion of 3-D crosshole seismic, radar, and ERT data followed by classification of zones and an over-determined inversion for zonal parameters. A zonation approach based on Gaussian mixtures was used to identify zones in the inversion models. Our synthetic example demonstrates how joint inversion reduces the misclassification rate from 21.3% for the individual inversions to 3.7% for the three-method joint inversion. The joint inversion zonal models also provide much better estimates of the zonal parameters (0.3% error compared to 1.8% using the individual inversion tomograms).

Our strategy of jointly inverting three types of 3-D data was applied to an active gravel aquifer adjacent to the Thur River in northern Switzerland. Clustering of the joint inversion tomograms produced noticeably better results than clustering of the individual inversion tomograms, primarily because of the clearer scatter plots obtained from the joint inversion models; the Gaussian mixture cluster estimation technique capitalized on this decreased scattering. The joint inversion and zonation models are complementary. The smooth joint inversion tomograms include information about lateral variability and general trends (e.g., decreasing resistivity with depth). The zonal representation summarizes important geometrical information about the aquifer and it enables petrophysical analysis at the field scale. The validity of the zonation can be assessed by zonal inversion for each method.

At our field site, we found three different sub-units within the gravel aquifer. The relative variation in porosity was estimated to be ~30% and the percentage of fine materials was found to increase with depth. The geometries and properties of the aquifer subunits determined here will be the starting point for hydrogeophysical modeling that will include data from extensive ongoing time-lapse ERT experiments at the same field site.

REFERENCES

Acworth, R. I., and Dasey, G. R., 2003. Mapping of the hyporheic zone around a tidal creek using a combination of borehole logging, borehole electrical tomography and cross-creek electrical imaging, New South Wales, Australia, *Hydrogeology Journal*, **11**, 368-377.

Ajo-Franklin, J. B., Minsley, B. J., and Daley, T. M., 2007. Applying compactness constraints to differential traveltime tomography, *Geophysics*, **72**, R67-R75.

al Hagrey, S. A., and Müller, C., 2000. GPR study of pore water content and salinity in sand, *Geophysical Prospecting*, **48**, 63-85.

Allègre, V., Jouniaux, L., Lehmann, F., and Sailhac, P., 2010. Streaming potential dependence on water-content in Fontainebleau sand, *Geophysical Journal International*, **182**, 1248-1266.

Alumbaugh, D., Chang, P. Y., Paprocki, L., Brainard, J. R., Glass, R. J., and Rautman, C. A., 2002. Estimating moisture contents in the vadose zone using cross-borehole ground penetrating radar: A study of accuracy and repeatability, *Water Resources Research*, **38**, 1309.

Alumbaugh, D. L., and Newman, G. A., 2000. Image appraisal for 2-D and 3-D electromagnetic inversion, *Geophysics*, **65**, 1455-1467.

Annan, A. P., 2005. GPR Methods for Hydrogeological Studies, in *Hydrogeophysics*, edited by Y. Rubin and S. S. Hubbard, pp. 185-213, Springer Netherlands.

Archie, G. E., 1942. The electrical resistivity log as an aid in determining some reservoir characteristics, *Transactions of the American institute of Mining, Metallurgical and Petroleum Engineers*, **146**, 54-62.

Arora, T., Linde, N., Revil, A., and Castermant, J., 2007. Non-intrusive characterization of the redox potential of landfill leachate plumes from self-potential data, *Journal of Contaminant Hydrology*, **92**, 274-292.

Aubert, M., and Yéené Atangana, Q., 1996. Self-potential method in hydrogeological exploration of volcanic areas, *Ground Water*, **34**, 1010-1016.

Avseth, P., Mukerji, T., Jørstad, A., Mavko, G., and Veggeland, T., 2001. Seismic reservoir mapping from 3-D AVO in a North Sea turbidite system, *Geophysics*, **66**, 1157-1176.

BAFU, 2010. Hydrologischer Atlas der Schweiz, *Bundeamt für Umwelt, Bern, Switzerland*.

Barrash, W., and Clemo, T., 2002. Hierarchical geostatistics and multifacies systems: Boise Hydrogeophysical Research Site, Boise, Idaho, *Water Resources Research*, **38**, 1196.

Barrenetxea, G., Ingelrest, F., Schaefer, G., and Vetterli, M., 2008. The hitchhiker's guide to successful wireless sensor network deployments, *Sensys'08: Proceedings of the 6th Acm Conference on Embedded Networked Sensor Systems*, 43-56.

Battin, T. J., and Sengschmitt, D., 1999. Linking sediment biofilms, hydrodynamics, and river bed clogging: Evidence from a large river, *Microbial Ecology*, **37**, 185-196.

Baumann, M., Jordan, P., Hoehn, E., and Geisser, H., 2009. Ein neues Grundwassermodell für das Thurtal, *Mitteilungen der Thurgauischen Naturforschenden Gesellschaft*, **63**.

Bedrosian, P. A., Maercklin, N., Weckmann, U., Bartov, Y., Ryberg, T., and Ritter, O., 2007. Lithology-derived structure classification from the joint interpretation of magnetotelluric and seismic models, *Geophysical Journal International*, **170**, 737-748.

Bélanger, C., Giroux, B., Gloaguen, E., and Lefebvre, R., 2010. GPR, ERT and CPT data integration for high resolution aquifer modeling, *13th International Conference on GPR*, 1-6.

Belghoul, A., 2007. *Caractérisation petrophysique et hydrodynamique du socle cristallin*: PhD thesis, University of Montpellier.

Belina, F. A., Ernst, J. R., and Holliger, K., 2009. Inversion of crosshole seismic data in heterogeneous environments: Comparison of waveform and ray-based approaches, *Journal of Applied Geophysics*, **68**, 85-94.

Bencala, K. E., 1984. Interactions of solutes and streambed sediment 2. A dynamic analysis of coupled hydrologic and chemical processes that determine solute transport, *Water Resources Research*, **20**, 1804-1814.

Beres, M., Green, A., Huggenberger, P., and Horstmeyer, H., 1995. Mapping the architecture of glaciofluvial sediments with 3-dimensional georadar, *Geology*, **23**, 1087-1090.

Beres, M., Huggenberger, P., Green, A. G., and Horstmeyer, H., 1999. Using two- and three-dimensional georadar methods to characterize glaciofluvial architecture, *Sedimentary Geology*, **129**, 1-24.

Bernhardt, E. S., Palmer, M. A., Allan, J. D., Alexander, G., Barnas, K., et al., 2005. Ecology - Synthesizing US river restoration efforts, *Science*, **308**, 636-637.

Beutel, J., Dyer, M., Lim, R., Plessl, C., Wohrle, M., et al., 2007. Automated wireless sensor network testing, *INSS 07: Proceedings of the Fourth International Conference on Networked Sensing Systems*, 303-303.

Beven, K., and Binley, A., 1992. The future of distributed models - model calibration and uncertainty prediction, *Hydrological Processes*, **6**, 279-298.

Bing, Z., and Greenhalgh, S. A., 1998a. A damping method for the computation of the 2.5-D Green's function for arbitrary acoustic media, *Geophysical Journal International*, **133**, 111-120.

Bing, Z., and Greenhalgh, S. A., 1998b. Crosshole acoustic velocity imaging with full-waveform spectral data: 2.5-D numerical simulations, *Exploration Geophysics*, **29**, 680-684.

Bing, Z., and Greenhalgh, S. A., 2000. Cross-hole resistivity tomography using different electrode configurations, *Geophysical Prospecting*, **48**, 887-912.

Binley, A., Winship, P., Middleton, R., Pokar, M., and West, J., 2001. High-resolution characterization of vadose zone dynamics using cross-borehole radar, *Water Resources Research*, **37**, 2639-2652.

Binley, A., Winship, P., West, L. J., Pokar, M., and Middleton, R., 2002a. Seasonal variation of moisture content in unsaturated sandstone inferred from borehole radar and resistivity profiles, *Journal of Hydrology*, **267**, 160-172.

Binley, A., Cassiani, G., Middleton, R., and Winship, P., 2002b. Vadose zone flow model parameterisation using cross-borehole radar and resistivity imaging, *Journal of Hydrology*, **267**, 147-159.

Binley, A., Cassiani, G., and Deiana, R., 2010. Hydrogeophysics: Opportunities and challenges, *Bollettino di Geofisica Teorica ed Applicata*, **51**, 267-284.

Birchak, J. R., Gardner, C. G., Hipp, J. E., and Victor, J. M., 1974. High dielectric constant microwave probes for sensing soil moisture, *Proceedings of the IEEE*, **62**, 93-98.

Bleistein, N., 1986. 2-1/2 dimensional inplane wave-propagation, *Geophysical Prospecting*, **34**, 686-703.

Blome, M., Maurer, H. R., and Schmidt, K., 2009. Advances in three-dimensional geoelectric forward solver techniques, *Geophysical Journal International*, **176**, 740-752.

Blome, M., Maurer, H., and Greenhalgh, S., 2011. Geoelectric experimental design - Efficient acquisition and exploitation of complete pole-bipole data sets, *Geophysics*, **76**, F15-F26.

Boggs, J. M., and Adams, E. E., 1992. Field study of dispersion in a heterogeneous aquifer: 4. Investigation of adsorption and sampling bias, *Water Resources Research*, **28**, 3325-3336.

Boggs, J. M., Young, S. C., Beard, L. M., Gelhar, L. W., Rehfeldt, K. R., and Adams, E. E., 1992. Field-study of dispersion in a heterogeneous aquifer: 1. Overview and site description, *Water Resources Research*, **28**, 3281-3291.

Bohlen, T., 2002. Parallel 3-D viscoelastic finite difference seismic modelling, *Computers & Geosciences*, **28**, 887-899.

Bolève, A., Revil, A., Janod, F., Mattiuzzo, J. L., and Fry, J. J., 2009. Preferential fluid flow pathways in embankment dams imaged by self-potential tomography, *Near Surface Geophysics*, **7**, 447-462.

Bosma, T. N. P., Ballemans, E. M. W., Hoekstra, N. K., teWelscher, R. A. G., Smeenk, J. G. M. M., et al., 1996. Biotransformation of organics in soil columns and an infiltration area, *Ground Water*, **34**, 49-56.

Bouman, C. A., 1997. Cluster: An unsupervised algorithm for modeling Gaussian mixtures, http://www.ece.purdue.edu/~bouman.

Bourg, A. C. M., and Bertin, C., 1993. Biogeochemical processes during the infiltration of river water into an alluvial aquifer, *Environmental Science & Technology*, **27**, 661-666.

Bouwer, H., and Rice, R. C., 1976. Slug test for determining hydraulic conductivity of unconfined aquifers with completely or partially penetrating wells, *Water Resources Research*, **12**, 423-428.

Bowling, J. C., Rodriguez, A. B., Harry, D. L., and Zheng, C., 2005. Delineating alluvial aquifer heterogeneity using resistivity and GPR data, *Ground Water*, **43**, 890-903.

Bowling, J. C., Harry, D. L., Rodriguez, A. B., and Zheng, C., 2007. Integrated geophysical and geological investigation of a heterogeneous fluvial aquifer in Columbus Mississippi, *Journal of Applied Geophysics*, **62**, 58-73.

Bradford, J. H., Clement, W. P., and Barrash, W., 2009. Estimating porosity with ground-penetrating radar reflection tomography: A controlled 3-D experiment at the Boise Hydrogeophysical Research Site, *Water Resources Research*, **45**, W00D26.

Brookes, A., 1988. *Channelized rivers: Prospectives for environmental management*, John Wiley and Sons, Chichester, UK.

Brovelli, A., and Cassiani, G., 2010. A combination of the Hashin-Shtrikman bounds aimed at modelling electrical conductivity and permittivity of variably saturated porous media, *Geophysical Journal International*, **180**, 225-237.

Brunke, M., and Gonser, T., 1997. The ecological significance of exchange processes between rivers and groundwater, *Freshwater Biology*, **37**, 1-33.

Butler, A. P., Mathias, S. A., Gallagher, A. J., Peach, D. W., and Williams, A. T., 2009. Analysis of flow processes in fractured chalk under pumped and ambient conditions (UK), *Hydrogeology Journal*, **17**, 1849-1858.

Butler, J. J., 1998. *The design, performance and analysis of slug tests*, Lewis, Boca Raton.

Butler, J. J., Garnett, E. J., and Healey, J. M., 2003. Analysis of slug tests in formations of high hydraulic conductivity, *Ground Water*, **41**, 620-630.

BUWAL, 2004. Wegleitung Grundwasserschutz, *Bundesamt für Umwelt, Wald und Landschaft, Bern, Switzerland*.

Carcione, J. M., Ursin, B., and Nordskag, J. I., 2007. Cross-property relations between electrical conductivity and the seismic velocity of rocks, *Geophysics*, **72**, E193-E204.

Cardenas, M. B., Wilson, J. L., and Zlotnik, V. A., 2004. Impact of heterogeneity, bed forms, and stream curvature on subchannel hyporheic exchange, *Water Resources Research*, **40**, W08307.

Cardenas, M. B., and Markowski, M. S., 2011. Geoelectrical imaging of hyporheic exchange and mixing of river water and groundwater in a large regulated river, *Environmental Science & Technology*, **45**, 1407-1411.

Carsel, R. F., and Parrish, R. S., 1988. Developing joint probability-distributions of soil-water retention characteristics, *Water Resources Research*, **24**, 755-769.

Caruthers, R. M., and Smith, I. F., 1992. The use of ground electrical survey methods for siting water-supply boreholes in shallow crystalline basement terrains, in *Hydrogeology of Crystalline Basement Aquifers in Africa*, edited by E. P. Wright and W. G. Burgess, pp. 203-220, Geological Society Special Publication.

Cassiani, G., Bruno, V., Villa, A., Fusi, N., and Binley, A. M., 2006. A saline trace test monitored via time-lapse surface electrical resistivity tomography, *Journal of Applied Geophysics*, **59**, 244-259.

Chambers, J. E., Wilkinson, P. B., Weller, A. L., Meldrum, P. I., Gilvy, R. D., and Caunt, S., 2007. Mineshaft imaging using surface and crosshole 3D electrical resistivity tomography: A case history from the East Pennine Coalfield, UK, *Journal of Applied Geophysics*, **62**, 324-337.

Chen, J. S., Hubbard, S., Rubin, Y., Murray, C., Roden, E., and Majer, E., 2004. Geochemical characterization using geophysical data and Markov Chain Monte Carlo methods: A case study at the South Oyster bacterial transport site in Virginia, *Water Resources Research*, **40**, W12412.

Cirpka, O. A., Fienen, M. N., Hofer, M., Hoehn, E., Tessarini, A., et al., 2007. Analyzing bank filtration by deconvoluting time series of electric conductivity, *Ground Water*, **45**, 318-328.

Claerbout, J. F., and Muir, F., 1973. Robust modeling with erratic data, *Geophysics*, **38**, 826-844.

Constantz, J., Cox, M. H., and Su, G. W., 2003. Comparison of heat and bromide as ground water tracers near streams, *Ground Water*, **41**, 647-656.

Constantz, J., 2008. Heat as a tracer to determine streambed water exchanges, *Water Resources Research*, **44**, W00D10.

Coscia, I., Marescot, L., Maurer, H., Greenhalgh, S., and Linde, N., 2008. Experimental design for crosshole electrical resistivity tomography data sets, *14th Annual European Meeting of Environmental and Engineering Geophysics, EAGE.*

Coscia, I., Greenhalgh, S., Linde, N., Green, A., Günther, T., et al., 2010. A multi-borehole 3-D ERT monitoring system for aquifer characterization using river flood events as a natural tracer, *16th Annual European Meeting of Environmental and Engineering Geophysics, EAGE.*

Coscia, I., Greenhalgh, S. A., Linde, N., Doetsch, J., Marescot, L., et al., 2011a. 3D crosshole ERT for aquifer characterization and monitoring of infiltrating river water, *Geophysics*, **76**, G49-G59.

Coscia, I., Linde, N., Greenhalgh, S., Günther, T., and Green, A., 2011b. A deconvolution approach to correct time-lapse 3D ERT data and improve imaging of natural aquifer dynamics, *Water Resources Research*, under review.

Crook, N., Binley, A., Knight, R., Robinson, D. A., Zarnetske, J., and Haggerty, R., 2008. Electrical resistivity imaging of the architecture of substream sediments, *Water Resources Research*, **44**, W00D13.

Daily, W., and Owen, E., 1991. Cross-borehole resistivity tomography, *Geophysics*, **56**, 1228-1235.

Daily, W., Ramirez, A., Labrecque, D., and Nitao, J., 1992. Electrical resistivity tomography of vadose water movement, *Water Resources Research*, **28**, 1429-1442.

Daily, W., and Ramirez, A., 1995. Electrical-resistance tomography during in-situ trichloroethylene remediation at the savanna river site, *Journal of Applied Geophysics*, **33**, 239-249.

Daily, W., Ramirez, A., Binley, A., and LaBrecque, D., 2005. Electrical resistance tomography — theory and practice, in *Near surface geophysics*, edited by D. K. Butler, pp. 525-550, SEG.

Daniels, J. J., Allred, B., Binley, A., Labrecque, D., and Alumbaugh, D., 2005. Hydrogeophysical case studies in the vadose zone, in *Hydrogeophysics*, edited by Y. Rubin and S. S. Hubbard, pp. 413-440, Springer.

Darling, T., 2005. *Well logging and formation evaluation*, Elsevier.

Darnet, M., and Marquis, G., 2004. Modelling streaming potential (SP) signals induced by water movement in the vadose zone, *Journal of Hydrology*, **285**, 114-124.

Day-Lewis, F. D., Lane, J. W., Jr., Harris, J. M., and Gorelick, S. M., 2003. Time-lapse imaging of saline-tracer transport in fractured rock using difference-attenuation radar tomography, *Water Resources Research*, **39**, 1290.

Day-Lewis, F. D., and Lane, J. W., 2004. Assessing the resolution-dependent utility of tomograms for geostatistics, *Geophysical Research Letters*, **31**, L07503.

Day-Lewis, F. D., Singha, K., and Binley, A. M., 2005. Applying petrophysical models to radar travel time and electrical resistivity tomograms: Resolution-dependent limitations, *Journal of Geophysical Research-Solid Earth*, **110**, B08206.

Day-Lewis, F. D., Lane, J. W., and Gorelick, S. M., 2006. Combined interpretation of radar, hydraulic, and tracer data from a fractured-rock aquifer near Mirror Lake, New Hampshire, USA, *Hydrogeology Journal*, **14**, 1-14.

Day-Lewis, F. D., Chen, Y., and Singha, K., 2007. Moment inference from tomograms, *Geophysical Research Letters*, **34**, L22404.

de Franco, R., Biella, G., Tosi, L., Teatini, P., Lozej, A., et al., 2009. Monitoring the saltwater intrusion by time lapse electrical resistivity tomography: The Chioggia test site (Venice Lagoon, Italy), *Journal of Applied Geophysics*, **69**, 117-130.

Deiana, R., Cassiani, G., Kemna, A., Villa, A., Bruno, V., and Bagliani, A., 2007. An experiment of non-invasive characterization of the vadose zone via water injection and cross-hole time-lapse geophysical monitoring, *Near Surface Geophysics*, **5**, 183-194.

Dempster, A. P., Laird, N. M., and Rubin, D. B., 1977. Maximum likelihood from incomplete data via the EM algorithm, *Journal of the Royal Statistical Society, Series B (Methodological)*, **39**, 1-38.

Deutsch, C. V., and Journel, A. G., 1998. *GSLIB: Geostatistical software library and user's guide*, 2. edition ed., Oxford Univ. Press, New York, 2. edition.

Diem, S., Vogt, T., and Hoehn, E., 2010. Räumliche Charakterisierung der hydraulischen Leitfähigkeit in alluvialen Schotter-Grundwasserleitern: Ein Methodenvergleich, *Grundwasser*, **15**, 241-251.

Dietrich, C. R., and Newsam, G. N., 1997. Fast and exact simulation of stationary Gaussian processes through circulant embedding of the covariance matrix, *Siam Journal on Scientific Computing*, **18**, 1088-1107.

Dogan, M., Van Dam, R. L., Bohling, G. C., Butler, J. J., Jr., and Hyndman, D. W., 2011. Hydrostratigraphic analysis of the MADE site with full-resolution GPR and direct-push hydraulic profiling, *Geophysical Research Letters*, **38**, L06405.

Dorn, C., Linde, N., Le Borgne, T., Bour, O., and Baron, L., 2011. Single-hole GPR reflection imaging of solute transport in a granitic aquifer, *Geophysical Research Letters*, **38**, L08401.

Doussan, C., Jouniaux, L., and Thony, J. L., 2002. Variations of self-potential and unsaturated water flow with time in sandy loam and clay loam soils, *Journal of Hydrology*, **267**, 173-185.

EC, 2000. Directive 2000/60/EC of the European Parliament and of the council establishing a framework for community action in the field of water policy, *Official Journal of the European Community*, **L327**, 1-72.

Eckert, P., Lamberts, R., and Wagner, C., 2008. The impact of climate change on drinking water supply by riverbank filtration, *Water Science Technology*, **8**, 319-324.

Edmaier, K., Burlando, P., and Perona, P., 2011. Mechanisms of vegetation uprooting by flow in alluvial non-cohesive sediment, *Hydrology and Earth Systems Science Discussion*, **8**, 1365-1398.

Eisenberg, D., and Kauzmann, W., 1969. *The structure and properties of water*, Oxford University Press.

Ellis, R. G., and Oldenburg, D. W., 1994. Applied geophysical inversion, *Geophysical Journal International*, **116**, 5-11.

Eppstein, M. J., and Dougherty, D. E., 1998. Optimal 3-D traveltime tomography, *Geophysics*, **63**, 1053-1061.

Ernst, J. R., Maurer, H., Green, A. G., and Holliger, K., 2007a. Full-waveform inversion of crosshole radar data based on 2-D finite-difference time-domain solutions of Maxwell's equations, *Ieee Transactions on Geoscience and Remote Sensing*, **45**, 2807-2828.

Ernst, J. R., Green, A. G., Maurer, H., and Holliger, K., 2007b. Application of a new 2D time-domain full-waveform inversion scheme to crosshole radar data, *Geophysics*, **72**, J53-J64.

Ernst, J. R., 2007. *2-D finite-difference time-domain full-waveform inversion of crosshole georadar data*: PhD thesis, ETH Zurich.

Farquharson, C. G., 2008. Constructing piecewise-constant models in multidimensional minimum-structure inversions, *Geophysics*, **73**, K1-K9.

Favetto, A., Pomposiello, C., Booker, J., and Rossello, E. A., 2007. Magnetotelluric inversion constrained by seismic data in the Tucuman basin (Andean foothills, 27 degrees S, NW argentina), *Journal of Geophysical Research - Solid Earth*, **112**, B09104.

Fine, R. A., and Millero, F. J., 1973. Compressibility of water as a function of temperature and pressure, *Journal of Chemical Physics*, **59**, 5529-5536.

Fleckenstein, J. H., Niswonger, R. G., and Fogg, G. E., 2006. River-aquifer interactions, geologic heterogeneity, and low-flow management, *Ground Water*, **44**, 837-852.

Fournier, C., 1989. Spontaneous potentials and resistivity surveys applied to hydrogeology in a volcanic area - case-history of the Chaine-Des-Puys (Puy-De-Dome, France), *Geophysical Prospecting*, **37**, 647-668.

Fregoso, E., and Gallardo, L. A., 2009. Cross-gradients joint 3D inversion with applications to gravity and magnetic data, *Geophysics*, **74**, L31-L42.

French, H., and Binley, A., 2004. Snowmelt infiltration: Monitoring temporal and spatial variability using time-lapse electrical resistivity, *Journal of Hydrology*, **297**, 174-186.

Friedel, S., 2003. Resolution, stability and efficiency of resistivity tomography estimated from a generalized inverse approach, *Geophysical Journal International*, **153**, 305-316.

Friedel, S., Byrdina, S., Jacobs, F., and Zimmer, M., 2004. Self-potential and ground temperature at Merapi volcano prior to its crisis in the rainy season of 2000-2001, *Journal of Volcanology and Geothermal Research*, **134**, 149-168.

Füchtenbauer, H., 1988. *Sedimente und Sedimentgesteine: Sandsteine*, 4 ed., Schweizerbart, Stuttgart.

Gallardo, L. A., and Meju, M. A., 2003. Characterization of heterogeneous near-surface materials by joint 2D inversion of dc resistivity and seismic data, *Geophysical Research Letters*, **30**, 1658.

Gallardo, L. A., and Meju, M. A., 2004. Joint two-dimensional DC resistivity and seismic travel time inversion with cross-gradients constraints, *Journal of Geophysical Research - Solid Earth*, **109**, B03311.

Gallardo, L. A., Meju, M. A., and Pérez-Flores, M. A., 2005. A quadratic programming approach for joint image reconstruction: Mathematical and geophysical examples, *Inverse Problems*, **21**, 435-452.

Gallardo, L. A., 2007. Multiple cross-gradient joint inversion for geospectral imaging, *Geophysical Research Letters*, **34**, L19301.

Gallardo, L. A., and Meju, M. A., 2007. Joint two-dimensional cross-gradient imaging of magnetotelluric and seismic traveltime data for structural and lithological classification, *Geophysical Journal International*, **169**, 1261-1272.

Gallardo, L. A., and Meju, M. A., 2011. Structure-Coupled Multiphysics Imaging in Geophysical Sciences, *Reviews of Geophysics*, **49**, RG1003.

Garambois, S., Senechal, P., and Perroud, H., 2002. On the use of combined geophysical methods to assess water content and water conductivity of near-surface formations, *Journal of Hydrology*, **259**, 32-48.

Gasperikova, E., Zhang, Y., and Hubbard, S., 2008. Using self potential and multiphase flow modeling to optimize groundwater pumping*, EOS Transactions AGU, 89(53).*

Giannopoulos, A., 2005. Modelling ground penetrating radar by GprMax, *Construction and Building Materials*, **19**, 755-762.

Gibert, D., and Pessel, M., 2001. Identification of sources of potential fields with the continuous wavelet transform: Application to self-potential profiles, *Geophysical Research Letters*, **28**, 1863-1866.

Golub, G. H., and van Loan, C. F., 1996. *Matrix computations*, Johns Hopkins University Press.

Gooseff, M. N., Anderson, J. K., Wondzell, S. M., LaNier, J., and Haggerty, R., 2005. A modelling study of hyporheic exchange pattern and the sequence, size, and spacing of stream bedforms in mountain stream networks, Oregon, USA, *Hydrological Processes*, **19**, 2915-2929.

Grasmueck, M., 1996. 3-D ground-penetrating radar applied to fracture imaging in gneiss, *Geophysics*, **61**, 1050-1064.

Grinsted, A., Moore, J. C., and Jevrejeva, S., 2004. Application of the cross wavelet transform and wavelet coherence to geophysical time series, *Nonlinear Processes in Geophysics*, **11**, 561-566.

GschG, 1991. Gewaesserschutzgesetz,, *Bundesgesetz über den Schutz der Gewässer, Schweiz*, **814.20**, 30.

GSchV, 1998. Gewaesserschutzverordnung, *Bundesgesetz über den Schutz der Gewässer, Schweiz*, **814.201**, 60.

Günther, T., 2004. *Inversion methods and resolution analysis for the 2D/3D reconstruction of resistivity structures from DC measurements*, Ph.D. thesis thesis: TU Bergakademie Freiberg.

Günther, T., and Rücker, C., 2006. A general approach for introducing information into inversion and examples from dc resistivity inversion, in *14th Annual European Meeting of Environmental and Engineering Geophysics*, edited, p. P039, EAGE.

Günther, T., Rücker, C., and Spitzer, K., 2006. Three-dimensional modelling and inversion of dc resistivity data incorporating topography - II. Inversion, *Geophysical Journal International*, **166**, 506-517.

Günther, T., and Rücker, C., 2009. Advanced inversion strategies using a new geophysical inversion and modelling library, *15th Annual European Meeting of Environmental and Engineering Geophysics, EAGE.*

Haber, E., and Oldenburg, D., 1997. Joint inversion: A structural approach, *Inverse Problems*, **13**, 63-77.

Harbaugh, A. W., 2005. MODFLOW-2005, The U.S. Geological Survey modular ground-water model—the ground-water flow process, in *Book 6. Modeling techniques*, Ch. 16.

Harvey, J. W., and Bencala, K. E., 1993. The effect of streambed topography on surface-subsurface water exchange in mountain catchments, *Water Resources Research*, **29**, 89-98.

Hashin, Z., and Shtrikman, S., 1962. A variational approach to theory of effective magnetic permeability of multiphase materials, *Journal of Applied Physics*, **33**, 3125-&.

Hashin, Z., and Shtrikman, S., 1963. A variational approach to the theory of the elastic behaviour of multiphase materials, *Journal of the Mechanics and Physics of Solids*, **11**, 127-140.

Hatch, C. E., Fisher, A. T., Revenaugh, J. S., Constantz, J., and Ruehl, C., 2006. Quantifying surface water-groundwater interactions using time series analysis of streambed thermal records: Method development, *Water Resources Research*, **42**, W10410.

Hauck, C., 2002. Frozen ground monitoring using DC resistivity tomography, *Geophysical Research Letters*, **29**, 2016.

Hayley, K., Bentley, L. R., and Gharibi, M., 2009. Time-lapse electrical resistivity monitoring of salt-affected soil and groundwater, *Water Resources Research*, **45**.

Heinz, J., Kleineidam, S., Teutsch, G., and Aigner, T., 2003. Heterogeneity patterns of quaternary glaciofluvial gravel bodies (SW-Germany): Application to hydrogeology, *Sedimentary Geology*, **158**, 1-23.

Henderson, R. D., Day-Lewis, F. D., and Harvey, C. F., 2009. Investigation of aquifer-estuary interaction using wavelet analysis of fiber-optic temperature data, *Geophysical Research Letters*, **36**, L06403.

Hiscock, K. M., and Grischek, T., 2002. Attenuation of groundwater pollution by bank filtration, *Journal of Hydrology*, **266**, 139-144.

Hoehn, E., and Cirpka, O. A., 2006. Assessing residence times of hyporheic ground water in two alluvial flood plains of the Southern Alps using water temperature and tracers, *Hydrology and Earth System Sciences*, **10**, 553-563.

Hoehn, E., and Scholtis, A., 2011. Exchange between a river and groundwater, assessed with hydrochemical data, *Hydrology and Earth System Sciences*, **15**, 983-988.

Hollender, F., Tillard, S., and Corin, L., 1999. Multifold borehole radar acquisition and processing, *Geophysical Prospecting*, **47**, 1077-1090.

Holliger, K., Musil, M., and Maurer, H. R., 2001. Ray-based amplitude tomography for crosshole georadar data: A numerical assessment, *Journal of Applied Geophysics*, **47**, 285-298.

Hu, W. Y., Abubakar, A., and Habashy, T. M., 2009. Joint electromagnetic and seismic inversion using structural constraints, *Geophysics*, **74**, R99-R109.

Hubbard, S., and Linde, N., 2011. Hydrogeophysics, in *Treatise on water*, edited by P. Wilderer, Ch. 43, Elsevier.

Hubbard, S. S., Rubin, Y., and Majer, E., 1999. Spatial correlation structure estimation using geophysical and hydrogeological data, *Water Resources Research*, **35**, 1809-1825.

Hubbard, S. S., Chen, J. S., Peterson, J., Majer, E. L., Williams, K. H., et al., 2001. Hydrogeological characterization of the South Oyster Bacterial Transport Site using geophysical data, *Water Resources Research*, **37**, 2431-2456.

Huggenberger, P., 1993. Radar facies: Recognition of facies patterns and heterogeneities within Pleistocene Rhine gravels, NE Switzerland, *Geological Society, London, Special Publications*, **75**, 163-176.

Huggenberger, P., Hoehn, E., Beschta, R., and Woessner, W., 1998. Abiotic aspects of channels and floodplains in riparian ecology, *Freshwater Biology*, **40**, 407-425.

Hyndman, D. W., and Gorelick, S. M., 1996. Estimating lithologic and transport properties in three dimensions using seismic and tracer data: The Kesterson aquifer, *Water Resources Research*, **32**, 2659-2670.

Hyndman, D. W., and Harris, J. M., 1996. Traveltime inversion for the geometry of aquifer lithologies, *Geophysics*, **61**, 1728-1737.

Jackson, M. D., 2010. Multiphase electrokinetic coupling: Insights into the impact of fluid and charge distribution at the pore scale from a bundle of capillary tubes model, *Journal of Geophysical Research-Solid Earth*, **115**, B07206.

Jacobs, L. A., Vongunten, H. R., Keil, R., and Kuslys, M., 1988. Geochemical changes along a river-groundwater infiltration flow path - Glattfelden, Switzerland, *Geochimica Et Cosmochimica Acta*, **52**, 2693-2706.

Jakubowicz, H., 1990. A simple efficient method of dip-moveout correction, *Geophysical Prospecting*, **38**, 221-245.

Jardani, A., Revil, A., Boleve, A., Crespy, A., Dupont, J. P., et al., 2007. Tomography of the Darcy velocity from self-potential measurements, *Geophysical Research Letters*, **34**, L24403.

Jayawickreme, D. H., Van Dam, R. L., and Hyndman, D. W., 2008. Subsurface imaging of vegetation, climate, and root-zone moisture interactions, *Geophysical Research Letters*, **35**, L18404.

Jegen, M. D., Hobbs, R. W., Tarits, P., and Chave, A., 2009. Joint inversion of marine magnetotelluric and gravity data incorporating seismic constraints: Preliminary results of sub-basalt imaging off the Faroe Shelf, *Earth and Planetary Science Letters*, **282**, 47-55.

Jougnot, D., Ghorbani, A., Revil, A., Leroy, P., and Cosenza, P., 2010. Spectral induced polarization of partially saturated clay-rocks: A mechanistic approach, *Geophysical Journal International*, **180**, 210-224.

Jung, H. K., Min, D. J., Lee, H. S., Oh, S., and Chung, H., 2009. Negative apparent resistivity in dipole-dipole electrical surveys, *Exploration Geophysics*, **40**, 33-40.

Kalbus, E., Reinstorf, F., and Schirmer, M., 2006. Measuring methods for groundwater - surface water interactions: A review, *Hydrology and Earth System Sciences*, **10**, 873-887.

Kalbus, E., Schmidt, C., Molson, J. W., Reinstorf, F., and Schirmer, M., 2009. Influence of aquifer and streambed heterogeneity on the distribution of groundwater discharge, *Hydrology and Earth System Sciences*, **13**, 69-77.

Keery, J., Binley, A., Crook, N., and Smith, J. W. N., 2007. Temporal and spatial variability of groundwater-surface water fluxes: Development and application of an analytical method using temperature time series, *Journal of Hydrology*, **336**, 1-16.

Keller, G. V., and Frischknecht, F., 1966. *Electrical methods in geophysical prospecting*, Pergamon.

Kemna, A., Kulessa, B., and Vereecken, H., 2002. Imaging and characterisation of subsurface solute transport using electrical resistivity tomography (ERT) and equivalent transport models, *Journal of Hydrology*, **267**, 125-146.

Khalil, A. A., Stewart, R. R., and Henley, D. C., 1993. Full-wave-form processing and interpretation of kilohertz cross-well seismic data, *Geophysics*, **58**, 1248-1256.

Kipfer, R., Aeschbach-Hertig, W., Peeters, F., and Stute, M., 2002. Noble gases in lakes and ground waters, *Noble Gases in Geochemistry and Cosmochemistry*, **47**, 615-700.

Klotzsche, A., van der Kruk, J., Meles, G. A., Doetsch, J., Maurer, H., and Linde, N., 2010. Full-waveform inversion of cross-hole ground-penetrating radar data to characterize a gravel aquifer close to the Thur River, Switzerland, *Near Surface Geophysics*, **8**, 635-649.

Knight, R. J., and Nur, A., 1987. The dielectric-constant of sandstones, 60 Khz to 4 Mhz, *Geophysics*, **52**, 644-654.

Koch, K., Wenninger, J., Uhlenbrook, S., and Bonell, M., 2009. Joint interpretation of hydrological and geophysical data: Electrical resistivity tomography results from a process hydrological research site in the Black Forest Mountains, Germany, *Hydrological Processes*, **23**, 1501-1513.

Kondolf, G. M., 1998. Lessons learned from river restoration projects in California, *Aquatic Conservation-Marine and Freshwater Ecosystems*, **8**, 39-52.

Kosinski, W. K., and Kelly, W. E., 1981. Geoelectric soundings for predicting aquifer properties, *Ground Water*, **19**, 163-171.

Kowalsky, M. B., Finsterle, S., Peterson, J., Hubbard, S., Rubin, Y., et al., 2005. Estimation of field-scale soil hydraulic and dielectric parameters through joint inversion of GPR and hydrological data, *Water Resources Research*, **41**, W11425.

Krautblatter, M., Verleysdonk, S., Flores-Orozco, A., and Kemna, A., 2010. Temperature-calibrated imaging of seasonal changes in permafrost rock walls by quantitative electrical resistivity tomography (Zugspitze, German/Austrian Alps), *Journal of Geophysical Research-Earth Surface*, **115**, F02003.

Kruse, S., Grasmueck, M., Weiss, M., and Viggiano, D., 2006. Sinkhole structure imaging in covered Karst terrain, *Geophysical Research Letters*, **33**, L16405.

Kumar, P., and Foufoula-Georgiou, E., 1997. Wavelet analysis for geophysical applications, *Reviews of Geophysics*, **35**, 385-412.

Kuras, O., Pritchard, J. D., Meldrum, P. I., Chambers, J. E., Wilkinson, P. B., et al., 2009. Monitoring hydraulic processes with automated time-lapse electrical resistivity tomography (ALERT), *Comptes Rendus Geoscience*, **341**, 868-885.

Kuroda, S., Takeuchi, M., and Kim, H. J., 2007. Full-waveform inversion algorithm for interpreting crosshole radar data: A theoretical approach, *Geosciences Journal*, **11**, 211-217.

LaBrecque, D. J., Ramirez, A. L., Daily, W. D., Binley, A. M., and Schima, S. A., 1996a. ERT monitoring on environmental remediation processes, *Measurement Science & Technology*, **7**, 375-383.

LaBrecque, D. J., Miletto, M., Daily, W., Ramirez, A., and Owen, E., 1996b. The effects of noise on Occam's inversion of resistivity tomography data, *Geophysics*, **61**, 538-548.

LaBrecque, D. J., and Yang, X., 2001. Difference inversion of ERT data: A fast inversion method for 3-D in situ monitoring, *Journal of Environmental and Engineering Geophysics*, **6**, 83-89.

Lacey, G., 1930. Stable channel in alluvium, *Proceedings of the Institution of Civil Engineers*, **229**, 259-292.

Lane, J. W., Day-Lewis, F. D., and Casey, C. C., 2006. Geophysical monitoring of a field-scale biostimulation pilot project, *Ground Water*, **44**, 430-443.

Langevin, C. D., Thorne, D. T., Jr., Dausman, A. M., Sukip, M. C., and Guo, W., 2008. SEAWAT version 4: A computer program for simulation of multi-species solute and heat transport, in *USGS Techniques and Methods Book 6*, Ch. A22.

Langevin, C. D., 2009. SEAWAT: A computer program for simulation of variable-density groundwater flow and multi-species solute and heat transport, *U.S. Geological Survey*, Fact Sheet 2009-3047.

Lanz, E., Boerner, D. E., Maurer, H., and Green, A., 1998. Landfill delineation and characterization using electrical, electromagnetic and magnetic methods, *Journal of Environmental and Engineering Geophysics*, **3**, 185-196.

Lazaratos, S. K., Harris, J. M., Rector, J. W., and Vanschaack, M., 1995. High-resolution crosswell imaging of a west texas carbonate reservoir 4. Reflection imaging, *Geophysics*, **60**, 702-711.

Le Borgne, T., Bour, O., Paillet, F. L., and Caudal, J. P., 2006. Assessment of preferential flow path connectivity, and hydraulic properties at single-borehole and cross-borehole scales in a fractured aquifer, *Journal of Hydrology*, **328**, 347-359.

Le Borgne, T., Bour, O., Riley, M. S., Gouze, P., Pezard, P. A., et al., 2007. Comparison of alternative methodologies for identifying and characterizing preferential flow paths in heterogeneous aquifers, *Journal of Hydrology*, **345**, 134-148.

Leonard, B. P., 1991. The ULTIMATE conservative difference scheme applied to unsteady one-dimensional advection, *Computer Methods in Applied Mechanics and Engineering*, **88**, 17-74.

Lesmes, D. P., and Friedman, S. P., 2005. Relationships between the electrical and hydrogeological properties of rocks and soils, in *Hydrogeophysics*, edited by Y. Rubin and S. S. Hubbard, pp. 87-128, Springer.

Li, S. H., Unsworth, M. J., Booker, J. R., Wei, W. B., Tan, H. D., and Jones, A. G., 2003. Partial melt or aqueous fluid in the mid-crust of Southern Tibet? Constraints from INDEPTH magnetotelluric data, *Geophysical Journal International*, **153**, 289-304.

Linde, N., Binley, A., Tryggvason, A., Pedersen, L. B., and Revil, A., 2006a. Improved hydrogeophysical characterization using joint inversion of cross-hole electrical resistance and ground-penetrating radar traveltime data, *Water Resources Research*, **42**, W12404.

Linde, N., Finsterle, S., and Hubbard, S., 2006b. Inversion of tracer test data using tomographic constraints, *Water Resources Research*, **42**, W04410.

Linde, N., Jougnot, D., Revil, A., Matthäi, S. K., Arora, T., et al., 2007a. Streaming current generation in two-phase flow conditions, *Geophysical Research Letters*, **34**, L03306.

Linde, N., and Revil, A., 2007. Inverting self-potential data for redox potentials of contaminant plumes, *Geophysical Research Letters*, **34**, L14302.

Linde, N., Revil, A., Bolève, A., Dagès, C., Castermant, J., et al., 2007b. Estimation of the water table throughout a catchment using self-potential and piezometric data in a Bayesian framework, *Journal of Hydrology*, **334**, 88-98.

Linde, N., Tryggvason, A., Peterson, J. E., and Hubbard, S. S., 2008. Joint inversion of crosshole radar and seismic traveltimes acquired at the South Oyster Bacterial Transport Site, *Geophysics*, **73**, G29-G37.

Linde, N., and Doetsch, J. A., 2010. Joint inversion of crosshole GPR and seismic traveltime data, in *Advances in near-surface seismology and ground-penetrating radar*, edited by R. D. Miller, J. H. Bradford and K. Holliger, Ch. 1, pp. 1-18, Society of Exploration Geophysicists.

Linde, N., Doetsch, J., Jougnot, D., Genoni, O., Dürst, Y., et al., 2011. Self-potential investigations of a gravel bar in a restored river corridor, *Hydrology and Earth System Sciences*, **15**, 729-742.

Lines, L. R., Schultz, A. K., and Treitel, S., 1988. Cooperative inversion of geophysical data, *Geophysics*, **53**, 8-20.

Loke, M. H., and Barker, R. D., 1996. Practical techniques for 3D resistivity surveys and data inversion, *Geophysical Prospecting*, **44**, 499-523.

Long, J. C. S., Aydin, A., Brown, S. R., Einstein, H. H., Hestir, K., et al., 1996. *Rock fracture and fluid flow: Contemporary understanding and applications*, National Academy Press, Washington, DC.

Looms, M. C., Jensen, K. H., Binley, A., and Nielsen, L., 2008. Monitoring unsaturated flow and transport using cross-borehole geophysical methods, *Vadose Zone Journal*, **7**, 227.

Lowry, T., Allen, M. B., and Shive, P. N., 1989. Singularity removal: A refinement of resistivity modeling techniques, *Geophysics*, **54**, 766-774.

Lunt, I. A., Bridge, J. S., and Tye, R. S., 2004. A quantitative three-dimensional depositional model of gravelly braided rivers, *Sedimentology*, **51**, 1155-1155.

Maineult, A., Bernabe, Y., and Ackerer, P., 2004. Electrical response of flow, diffusion, and advection in a laboratory sand box, *Vadose Zone Journal*, **3**, 1180-1192.

Maineult, A., Bernabe, Y., and Ackerer, P., 2005. Detection of advected concentration and pH fronts from self-potential measurements, *Journal of Geophysical Research-Solid Earth*, **110**, B11205.

Maineult, A., Strobach, E., and Renner, J., 2008. Self-potential signals induced by periodic pumping tests, *Journal of Geophysical Research-Solid Earth*, **113**, B01203.

Mair, J. A., and Green, A. G., 1981. High-resolution seismic-reflection profiles reveal fracture-zones within a homogeneous granite batholith, *Nature*, **294**, 439-442.

Maraun, D., and Kurths, J., 2004. Cross wavelet analysis: Significance testing and pitfalls, *Nonlinear Processes in Geophysics*, **11**, 505-514.

Marescot, L., Rigobert, S., P. Lopes, S., Lagabrielle, R., and Chapellier, D., 2006. A general approach for DC apparent resistivity evaluation on arbitrarily shaped 3D structures, *Journal of Applied Geophysics*, **60**, 55-67.

Maurer, H., Holliger, K., and Boerner, D. E., 1998. Stochastic regularization: Smoothness or similarity?, *Geophysical Research Letters*, **25**, 2889-2892.

Maurer, H., and Musil, M., 2004. Effects and removal of systematic errors in crosshole georadar attenuation tomography, *Journal of Applied Geophysics*, **55**, 261-270.

Maurer, H., and Friedel, S., 2006. Outer-space sensitivities in geoelectrical tomography, *Geophysics*, **71**, G93-G96.

Maurer, H., Friedel, S., and Jaeggi, D., 2009. Characterization of a coastal aquifer using seismic and geoelectric borehole methods, *Near Surface Geophysics*, **7**, 353-366.

Mazac, O., Kelly, W. E., and Landa, I., 1987. Surface geoelectrics for groundwater pollution and protection studies, *Journal of Hydrology*, **93**, 277-294.

McClymont, A. F., Green, A. G., Streich, R., Horstmeyer, H., Tronicke, J., et al., 2008. Visualization of active faults using geometric attributes of 3D GPR data: An example from the Alpine Fault Zone, New Zealand, *Geophysics*, **73**, B11-B23.

McElwee, C. D., and Zenner, M. A., 1998. A nonlinear model for analysis of slug-test data, *Water Resources Research*, **34**, 55-66.

Meles, G. A., Van der Kruk, J., Greenhalgh, S. A., Ernst, J. R., Maurer, H., and Green, A. G., 2010. A new vector waveform inversion algorithm for simultaneous updating of conductivity and permittivity parameters from combination crosshole/borehole-to-surface GPR data, *Ieee Transactions on Geoscience and Remote Sensing*, **48**, 3391-3407.

Merkli, B., 1975. *Untersuchungen über Mechanismen und Kinetik der Elimination von Bakterien und Viren im Grundwasser*: ETH Zurich.

Miall, A. D., 1995. Description and interpretation of fluvial deposits - A critical perspective, *Sedimentology*, **42**, 379-384.

Michel, S., Salehi, A., Luo, L., Dawes, N., Aberer, K., et al., 2009. Environmental monitoring 2.0, *Icde: 2009 Ieee 25th International Conference on Data Engineering, Vols. 1-3*, 1507-1510.

Michot, D., Benderitter, Y., Dorigny, A., Nicoullaud, B., King, D., and Tabbagh, A., 2003. Spatial and temporal monitoring of soil water content with an irrigated corn crop cover using surface electrical resistivity tomography, *Water Resources Research*, **39**, 1138.

Miller, C. R., Routh, P. S., Brosten, T. R., and McNamara, J. P., 2008. Application of time-lapse ERT imaging to watershed characterization, *Geophysics*, **73**, G7-G17.

Minsley, B. J., 2007. *Modeling and inversion of self-potential data*: PhD thesis, Massachusetts Institute of Technology.

Minsley, B. J., Sogade, J., and Morgan, F. D., 2007. Three-dimensional source inversion of self-potential data, *Journal of Geophysical Research*, **112**.

Mitchell, T. M., 1997. *Machine learning*, McGraw-Hill, New York.

Monego, M., Cassiani, G., Deiana, R., Putti, M., Passadore, G., and Altissimo, L., 2010. A tracer test in a shallow heterogeneous aquifer monitored via time-lapse surface electrical resistivity tomography, *Geophysics*, **75**, WA61-WA73.

Monteiro Santos, F. A., Sultan, S. A., Represas, P., and El Sorady, A. L., 2006. Joint inversion of gravity and geoelectrical data for groundwater and structural investigation: Application to the northwestern part of Sinai, Egypt, *Geophysical Journal International*, **165**, 705-718.

Mora, P., 1987. Nonlinear two-dimensional elastic inversion of multioffset seismic data, *Geophysics*, **52**, 1211-1228.

Müller, K., Vanderborght, J., Englert, A., Kemna, A., Huisman, J. A., et al., 2010. Imaging and characterization of solute transport during two tracer tests in a shallow aquifer using electrical resistivity tomography and multilevel groundwater samplers, *Water Resources Research*, **46**, W03502.

Musil, M., Maurer, H. R., and Green, A. G., 2003. Discrete tomography and joint inversion for loosely connected or unconnected physical properties: Application to crosshole seismic and georadar data sets, *Geophysical Journal International*, **153**, 389-402.

Nadeau, D. F., Brutsaert, W., Parlange, M. B., Bou-Zeid, E., Barrenetxea, G., et al., 2009. Estimation of urban sensible heat flux using a dense wireless network of observations, *Environmental Fluid Mechanics*, **9**, 635-653.

Nimmer, R. E., Osiensky, J. L., Binley, A. M., Sprenke, K. F., and Williams, B. C., 2007. Electrical resistivity imaging of conductive plume dilution in fractured rock, *Hydrogeology Journal*, **15**, 877-890.

Nimmer, R. E., Osiensky, J. L., Binley, A. M., and Williams, B. C., 2008. Three-dimensional effects causing artifacts in two-dimensional, cross-borehole, electrical imaging, *Journal of Hydrology*, **359**, 59-70.

Nyquist, J. E., Freyer, P. A., and Toran, L., 2008. Stream bottom resistivity tomography to map ground water discharge, *Ground Water*, **46**, 561-569.

Ogilvy, R. D., Meldrum, P. I., Kuras, O., Wilkinson, P. B., Chambers, J. E., et al., 2009. Automated monitoring of coastal aquifers with electrical resistivity tomography, *Near Surface Geophysics*, **7**, 367-375.

Oldenburg, D. W., and Li, Y. G., 1999. Estimating depth of investigation in dc resistivity and IP surveys, *Geophysics*, **64**, 403-416.

Olsson, O., Falk, L., Forslund, O., Lundmark, L., and Sandberg, E., 1992. Borehole radar applied to the characterization of hydraulically conductive fracture-zones in crystalline rock, *Geophysical Prospecting*, **40**, 109-142.

Oreskes, N., Shrader-Frechette, K., and Belitz, K., 1994. Verification, validation, and confirmation of numerical models in the earth sciences, *Science*, **263**, 641-646.

Orghidan, T., 1959. Ein neuer Lebensraum des unterirdischen Wassers: der hyporheische Biotop, *Arch. Hydrobiol.*, **55**, 392-414.

Osiensky, J. L., Nimmer, R., and Binley, A. M., 2004. Borehole cylindrical noise during hole-surface and hole-hole resistivity measurements, *Journal of Hydrology*, **289**, 78-94.

Paasche, H., Tronicke, J., Holliger, K., Green, A. G., and Maurer, H., 2006. Integration of diverse physical-property models: Subsurface zonation and petrophysical parameter estimation based on fuzzy c-means cluster analyses, *Geophysics*, **71**, H33-H44.

Paasche, H., and Tronicke, J., 2007. Cooperative inversion of 2D geophysical data sets: A zonal approach based on fuzzy c-means cluster analysis, *Geophysics*, **72**, A35-A39.

Paasche, H., Wendrich, A., Tronicke, J., and Trela, C., 2008. Detecting voids in masonry by cooperatively inverting P-wave and georadar traveltimes, *Journal of Geophysics and Engineering*, **5**, 256-267.

Paige, C. C., and Saunders, M. A., 1982. LSQR: An algorithm for sparse linear equations and sparse least squares, *ACM Transactions on Mathematical Software*, **8**, 43-71.

Palmer, M. A., Bernhardt, E. S., Allan, J. D., Lake, P. S., Alexander, G., et al., 2005. Standards for ecologically successful river restoration, *Journal of Applied Ecology*, **42**, 208-217.

Park, S. K., Johnston, M. J. S., Madden, T. R., Morgan, F. D., and Morrison, H. F., 1993. Electromagnetic precursors to earthquakes in the ULF band - a review of observations and mechanisms, *Reviews of Geophysics*, **31**, 117-132.

Parker, R. L., 1984. The inverse problem of resistivity sounding, *Geophysics*, **49**, 2143-2158.

Pasquale, N., Perona, P., Schneider, P., Shrestha, J., Wombacher, A., and Burlando, P., 2011. Modern comprehensive approach to monitor the morphodynamic evolution of a restored river corridor, *Hydrology and Earth System Sciences*, **15**, 1197-1212.

Perrier, F., and Morat, P., 2000. Characterization of electrical daily variations induced by capillary flow in the non-saturated zone, *Pure and Applied Geophysics*, **157**, 785-810.

Petiau, G., 2000. Second generation of lead-lead chloride electrodes for geophysical applications, *Pure and Applied Geophysics*, **157**, 357-382.

Podvin, P., and Lecomte, I., 1991. Finite difference computation of traveltimes in very contrasted velocity models: A massively parallel approach and its associated tools, *Geophysical Journal International*, **105**, 271-284.

Pollock, D., and Cirpka, O. A., 2010. Fully coupled hydrogeophysical inversion of synthetic salt tracer experiments, *Water Resources Research*, **46**, W07501.

Portniaguine, O., and Zhdanov, M. S., 1999. Focusing geophysical inversion images, *Geophysics*, **64**, 874-887.

Pratt, R. G., 1999. Seismic waveform inversion in the frequency domain, part 1: Theory and verification in a physical scale model, *Geophysics*, **64**, 888-901.

Pratt, R. G., and Shipp, R. M., 1999. Seismic waveform inversion in the frequency domain, part 2: Fault delineation in sediments using crosshole data, *Geophysics*, **64**, 902-914.

Pride, S., 1994. Governing equations for the coupled electromagnetics and acoustics of porous-media, *Physical Review B*, **50**, 15678-15696.

Pride, S. R., Berryman, J. G., and Harris, J. M., 2004. Seismic attenuation due to wave-induced flow, *Journal of Geophysical Research-Solid Earth*, **109**, B01201.

Pruess, K., Oldenburg, C. M., and Moridis, G. J., 1999. TOUGH2 user's guide version 2, Rep. LBNL--43134, 204 pp, Lawrence Berkeley National Laboratory.

Ptak, T., and Teutsch, G., 1994. Forced and natural gradient tracer tests in a highly heterogeneous porous aquifer - instrumentation and measurements, *Journal of Hydrology*, **159**, 79-104.

Ramirez, A., Daily, W., Labrecque, D., Owen, E., and Chesnut, D., 1993. Monitoring an underground steam injection process using electrical-resistance tomography, *Water Resources Research*, **29**, 73-87.

Ranguelova, E. B., 2002. *Segmentation of textured images on three-dimensional lattices*: PhD thesis, University of Dublin.

RECORD, 2011. Assessment and modeling of coupled ecological and hydrological dynamics in the restored corridor of the river, *Competence Center Environment and Sustainability*, http://www.cces.ethz.ch/projects/nature/Record.

Regli, C., Rauber, M., and Huggenberger, P., 2003. Analysis of aquifer heterogeneity within a well capture zone, comparison of model data with field experiments: A case study from the river Wiese, Switzerland, *Aquatic Sciences*, **65**, 111-128.

Revil, A., Cathles, L. M., Losh, S., and Nunn, J. A., 1998. Electrical conductivity in shaly sands with geophysical applications, *Journal of Geophysical Research - Solid Earth*, **103**, 23925-23936.

Revil, A., and Cathles, L. M., 1999. Permeability of shaly sands, *Water Resources Research*, **35**, 651-662.

Revil, A., Naudet, V., Nouzaret, J., and Pessel, M., 2003. Principles of electrography applied to self-potential electrokinetic sources and hydrogeological applications, *Water Resources Research*, **39**, 1114.

Revil, A., and Leroy, P., 2004. Constitutive equations for ionic transport in porous shales, *Journal of Geophysical Research-Solid Earth*, **109**, B03208.

Revil, A., and Linde, N., 2006. Chemico-electromechanical coupling in microporous media, *Journal of Colloid and Interface Science*, **302**, 682-694.

Revil, A., Linde, N., Cerepi, A., Jougnot, D., Matthai, S., and Finsterle, S., 2007. Electrokinetic coupling in unsaturated porous media, *Journal of Colloid and Interface Science*, **313**, 315-327.

Revil, A., Trolard, F., Bourrie, G., Castermant, J., Jardani, A., and Mendonca, C. A., 2009. Ionic contribution to the self-potential signals associated with a redox front, *Journal of Contaminant Hydrology*, **109**, 27-39.

Rizzo, E., Suski, B., Revil, A., Straface, S., and Troisi, S., 2004. Self-potential signals associated with pumping tests experiments, *Journal of Geophysical Research-Solid Earth*, **109**, B10203.

Robinson, D. A., Binley, A., Crook, N., Day-Lewis, F. D., Ferre, T. P. A., et al., 2008. Advancing process-based watershed hydrological research using near-surface geophysics: A vision for, and review of, electrical and magnetic geophysical methods, *Hydrological Processes*, **22**, 3604-3635.

Rubin, Y., and Hubbard, S. S. (Eds.), 2005. *Hydrogeophysics*, Springer, Dordrecht, The Netherlands.

Rücker, C., Günther, T., and Spitzer, K., 2006. Three-dimensional modelling and inversion of dc resistivity data incorporating topography - I. Modelling, *Geophysical Journal International*, **166**, 495-505.

Ruelleu, S., Moreau, F., Bour, O., Gapais, D., and Martelet, G., 2010. Impact of gently dipping discontinuities on basement aquifer recharge: An example from Ploemeur (Brittany, France), *Journal of Applied Geophysics*, **70**, 161-168.

Samaritani, E., Shrestha, J., Fournier, B., Frossard, E., Gillet, F., et al., 2011. Heterogeneity of soil carbon pools and fluxes in a channelized and a restored floodplain section (Thur River, Switzerland), *Hydrology and Earth System Sciences Discussions*, **8**, 1059-1091.

Sambridge, M., Braun, J., and Mcqueen, H., 1995. Geophysical parametrization and interpolation of irregular data using natural neighbors, *Geophysical Journal International*, **122**, 837-857.

Sandberg, S. K., Slater, L. D., and Versteeg, R., 2002. An integrated geophysical investigation of the hydrogeology of an anisotropic unconfined aquifer, *Journal of Hydrology*, **267**, 227-243.

Saracco, G., Labazuy, P., and Moreau, F., 2004. Localization of self-potential sources in volcano-electric effect with complex continuous wavelet transform and electrical tomography methods for an active volcano, *Geophysical Research Letters*, **31**, L12610.

Schälchli, U., 1992. The clogging of coarse gravel river beds by fine sediment, *Hydrobiologia*, **235-236**, 189-197.

Schälchli, U., 2008. Geschiebehaushalt im Thurgebiet, *Wasser Energie Luft*, **100**, 23-28.

Schäppi, B., Perona, P., Schneider, P., and Burlando, P., 2010. Integrating river cross section measurements with digital terrain models for improved flow modelling applications, *Computers & Geosciences*, **36**, 707-716.

Scheibe, T. D., and Chien, Y. J., 2003. An evaluation of conditioning data for solute transport prediction, *Ground Water*, **41**, 128-141.

Schmidt, C., Bayer-Raich, M., and Schirmer, M., 2006. Characterization of spatial heterogeneity of groundwater-stream water interactions using multiple depth streambed temperature measurements at the reach scale, *Hydrology and Earth System Sciences*, **10**, 849-859.

Schmidt, C., Conant, B., Bayer-Raich, M., and Schirmer, M., 2007. Evaluation and field-scale application of an analytical method to quantify groundwater discharge using mapped streambed temperatures, *Journal of Hydrology*, **347**, 292-307.

Schneider, P., Vogt, T., Schirmer, M., Doetsch, J., Linde, N., et al., 2011. Towards improved instrumentation for assessing river-groundwater interactions in a restored river corridor, *Hydrology and Earth System Sciences*, **15**, 2531-2549.

Schön, J. H., 1996. *Physical properties of rocks: Fundamentals and principles of petrophysics*, Elsevier Science Publishing Company, Inc.

Schulmeister, M. K., Butler, J. J., Healey, J. M., Zheng, L., Wysocki, D. A., and McCall, G. W., 2003. Direct-push electrical conductivity logging for high-resolution hydrostratigraphic characterization, *Ground Water Monitoring and Remediation*, **23**, 52-62.

Schwarzenbach, R. P., and Westall, J., 1981. Transport of non-polar organic-compounds from surface-water to groundwater - Laboratory sorption studies, *Environmental Science & Technology*, **15**, 1360-1367.

Schwarzenbach, R. P., Giger, W., Hoehn, E., and Schneider, J. K., 1983. Behavior of organic-compounds during infiltration of river water to groundwater - Field studies, *Environmental Science & Technology*, **17**, 472-479.

Schwarzenbach, R. P., Escher, B. I., Fenner, K., Hofstetter, T. B., Johnson, C. A., et al., 2006. The challenge of micropollutants in aquatic systems, *Science*, **313**, 1072-1077.

Seiz, G., and Foppa, N., 2007. Nationales Klima-Beobachtungssystem (GCOS Schweiz), *Bundesamt für Meteorologie und Klimatologie, MeteoSchweiz und ProClim, Bern, Switzerland*.

Selker, J. S., Thevenaz, L., Huwald, H., Mallet, A., Luxemburg, W., et al., 2006. Distributed fiber-optic temperature sensing for hydrologic systems, *Water Resources Research*, **42**, W12202.

Sen, P. N., Scala, C., and Cohen, M. H., 1981. A self-similar model for sedimentary-rocks with application to the dielectric-constant of fused glass-beads, *Geophysics*, **46**, 781-795.

Shankar, V., Eckert, P., Ojha, C. S. P., and Konig, C. M., 2009. Transient three-dimensional modeling of riverbank filtration at Grind well field, Germany, *Hydrogeology Journal*, **17**, 321-326.

Sheffer, M. R., and Oldenburg, D. W., 2007. Three-dimensional modelling of streaming potential, *Geophysical Journal International*, **169**, 839-848.

Sill, W. R., 1983. Self-potential modeling from primary flows, *Geophysics*, **48**, 76-86.

Silliman, S. E., and Booth, D. F., 1993. Analysis of time-series measurements of sediment temperature for identification of gaining vs losing portions of Juday-Creek, Indiana, *Journal of Hydrology*, **146**, 131-148.

Singha, K., and Gorelick, S. M., 2005. Saline tracer visualized with three-dimensional electrical resistivity tomography: Field-scale spatial moment analysis, *Water Resources Research*, **41**, W05023.

Sjödahl, P., Dahlin, T., and Johansson, S., 2009. Embankment dam seepage evaluation from resistivity monitoring data, *Near Surface Geophysics*, **7**, 463-474.

Slater, L., and Sandberg, S. K., 2000. Resistivity and induced polarization monitoring of salt transport under natural hydraulic gradients, *Geophysics*, **65**, 408-420.

Slater, L., Binley, A. M., Daily, W., and Johnson, R., 2000. Cross-hole electrical imaging of a controlled saline tracer injection, *Journal of Applied Geophysics*, **44**, 85-102.

Slater, L., and Binley, A., 2006. Synthetic and field-based electrical imaging of a zerovalent iron barrier: Implications for monitoring long-term barrier performance, *Geophysics*, **71**, B129-B137.

Slob, E., Sato, M., and Olhoeft, G., 2010. Surface and borehole ground-penetrating-radar developments, *Geophysics*, **75**, A103-A120.

Smith, D. G., and Jol, H. M., 1992. Ground-penetrating radar investigation of a Lake Bonneville delta, Provo level, Brigham City, Utah, *Geology*, **20**, 1083-1086.

Soar, P. J., and Thorne, C. R., 2001. *Channel restoration design for meandering rivers*, U.S. Army Engineer Research and Development Center, Vicksburg, Miss.

Spillmann, T., Maurer, H., Willenberg, H., Evans, K. F., Heincke, B., and Green, A. G., 2007. Characterization of an unstable rock mass based on borehole logs and diverse borehole radar data, *Journal of Applied Geophysics*, **61**, 16-38.

Springer, R. K., and Gelhar, L. W., 1991. Characterization of large-scale aquifer heterogeneity in glacial outwash by analysis of slug tests with oscillatory response, *US Geological Survey, Cape Cod*, Report 91-4034.

Stanford, J. A., and Ward, J. V., 1988. The hyporheic habitat of river ecosystems, *Nature*, **335**, 64-66.

Stanford, J. A., and Ward, J. V., 1993. An ecosystem perspective of alluvial rivers - connectivity and the hyporheic corridor, *Journal of the North American Benthological Society*, **12**, 48-60.

Stauffer, F., and Dracos, T., 1986. Experimental and numerical study of water and solute infiltration in layered porous-media, *Journal of Hydrology*, **84**, 9-34.

Storey, R. G., Howard, K. W. F., and Williams, D. D., 2003. Factors controlling riffle-scale hyporheic exchange flows and their seasonal changes in a gaining stream: A three-dimensional groundwater flow model, *Water Resources Research*, **39**, 1034.

Streich, R., van der Kruk, J., and Green, A. G., 2006. Three-dimensional multicomponent georadar imaging of sedimentary structures, *Near Surface Geophysics*, **4**, 39-48.

Streich, R., and van der Kruk, J., 2007a. Accurate imaging of multicomponent GPR data based on exact radiation patterns, *Ieee Transactions on Geoscience and Remote Sensing*, **45**, 93-103.

Streich, R., and van der Kruk, J., 2007b. Characterizing a GPR antenna system by near-field electric field measurements, *Geophysics*, **72**, A51-A55.

Stummer, P., Maurer, H., and Green, A. G., 2004. Experimental design: Electrical resistivity data sets that provide optimum subsurface information, *Geophysics*, **69**, 120-139.

Suski, B., Revil, A., Titov, K., Konosavsky, P., Voltz, M., et al., 2006. Monitoring of an infiltration experiment using the self-potential method, *Water Resources Research*, **42**, W08418.

SVGW, 2004. Jahrbuch 2003/2004, *SVGW, Zürich*.

SVGW, 2007. Empfehlungen – Revitalisierung im Einflussbereich von Trinkwasserfassungen, *Zürich, Switzerland*.

Talley, J., Baker, G. S., Becker, M. W., and Beyrle, N., 2005. Four dimensional mapping of tracer channelization in subhorizontal bedrock fractures using surface ground penetrating radar, *Geophysical Research Letters*, **32**, L04401.

Tarantola, A., 1984a. Inversion of seismic-reflection data in the acoustic approximation, *Geophysics*, **49**, 1259-1266.

Tarantola, A., 1984b. Linearized inversion of seismic-reflection data, *Geophysical Prospecting*, **32**, 998-1015.

Tarantola, A., 1986. A strategy for nonlinear elastic inversion of seismic-reflection data, *Geophysics*, **51**, 1893-1903.

Thony, J. L., Morat, P., Vachaud, G., and LeMouel, J. L., 1997. Field characterization of the relationship between electrical potential gradients and soil water flux, *Comptes Rendus De L'Academie Des Sciences*, **325**, 317-321.

Topp, G. C., Davis, J. L., and Annan, A. P., 1980. Electromagnetic determination of soil-water content - Measurements in coaxial transmission-lines, *Water Resources Research*, **16**, 574-582.

Topp, G. C., Davis, J. L., and Annan, A. P., 1982. Electromagnetic determination of soil-water content using TDR 2. Evaluation of installation and configuration of parallel transmission-lines, *Soil Science Society of America Journal*, **46**, 678-684.

Torrence, C., and Compo, G. P., 1998. A practical guide to wavelet analysis, *Bulletin of the American Meteorological Society*, **79**, 61-78.

Touchard, F., 1999. *Caractérisation hydrogéologique d'un aquifère en socle fracture. Site de Ploëmeur (Morbihan)*: PhD thesis, University of Rennes I.

Trefry, M. G., and Muffels, C., 2007. Feflow: A finite-element ground water flow and transport modeling tool, *Ground Water*, **45**, 525-528.

Triska, F. J., Kennedy, V. C., Avanzino, R. J., Zellweger, G. W., and Bencala, K. E., 1989. Retention and transport of nutrients in a 3rd-order stream in Northwestern California - hyporheic processes, *Ecology*, **70**, 1893-1905.

Triska, F. J., Duff, J. H., and Avanzino, R. J., 1993a. Patterns of hydrological exchange and nutrient transformation in the hyporheic zone of a gravel-bottom stream - examining terrestrial aquatic linkages, *Freshwater Biology*, **29**, 259-274.

Triska, F. J., Duff, J. H., and Avanzino, R. J., 1993b. The role of water exchange between a stream channel and its hyporheic zone in nitrogen cycling at the terrestrial aquatic interface, *Hydrobiologia*, **251**, 167-184.

Tronicke, J., Dietrich, P., Wahlig, U., and Appel, E., 2002. Integrating surface georadar and crosshole radar tomography: A validation experiment in braided stream deposits, *Geophysics*, **67**, 1516-1523.

Tronicke, J., and Holliger, K., 2004. Effects of gas- and water-filled boreholes on the amplitudes of crosshole georadar data as inferred from experimental evidence, *Geophysics*, **69**, 1255-1260.

Tronicke, J., Holliger, K., Barrash, W., and Knoll, M. D., 2004. Multivariate analysis of cross-hole georadar velocity and attenuation tomograms for aquifer zonation, *Water Resources Research*, **40**, W01519.

Trubilowicz, J., Cai, K., and Weiler, M., 2009. Viability of motes for hydrological measurement, *Water Resources Research*, **45**, W00D22.

Trush, W. J., McBain, S. M., and Leopold, L. B., 2000. Attributes of an alluvial river and their relation to water policy and management, *Proceedings of the National Academy of Sciences of the United States of America*, **97**, 11858-11863.

Tryggvason, A., Rögnvaldsson, S. T., and Flóvenz, Ó. G., 2002. Three-dimensional imaging of the P- and S-wave velocity structure and earthquake locations beneath Southwest Iceland, *Geophysical Journal International*, **151**, 848-866.

Tryggvason, A., and Linde, N., 2006. Local earthquake (LE) tomography with joint inversion for P- and S-wave velocities using structural constraints, *Geophysical Research Letters*, **33**, L07303.

Tryggvason, A., and Bergman, B., 2006. A traveltime reciprocity discrepancy in the Podvin & Lecomte time3d finite difference algorithm, *Geophysical Journal International*, **165**, 432-435.

Tsoflias, G. P., Halihan, T., and Sharp, J. M., 2001. Monitoring pumping test response in a fractured aquifer using ground-penetrating radar, *Water Resources Research*, **37**, 1221-1229.

Tsoflias, G. P., and Becker, M. W., 2008. Ground-penetrating-radar response to fracture-fluid salinity: Why lower frequencies are favorable for resolving salinity changes, *Geophysics*, **73**, J25-J30.

Tubino, M., and Seminara, G., 1990. Free forced interactions in developing meanders and suppression of free bars, *Journal of Fluid Mechanics*, **214**, 131-159.

Tufenkji, N., Ryan, J. N., and Elimelech, M., 2002. The promise of bank filtration, *Environmental Science & Technology*, **36**, 422A-428A.

Turesson, A., 2006. Water content and porosity estimated from ground-penetrating radar and resistivity, *Journal of Applied Geophysics*, **58**, 99-111.

van Genuchten, M. T., 1980. A closed-form equation for predicting the hydraulic conductivity of unsaturated soils, *Soil Science Society of America Journal*, **44**, 892-898.

Vasco, D. W., Peterson, J. E., and Majer, E. L., 1995. Beyond ray tomography - Wavepaths and fresnel volumes, *Geophysics*, **60**, 1790-1804.

Vereecken, H., Binley, A., Cassiani, G., Revil, A., and Titov, K. (Eds.), 2006. *Applied hydrogeophysics*, Springer, Dordrecht, The Netherlands.

Vereecken, H., Huisman, J. A., Bogena, H., Vanderborght, J., Vrugt, J. A., and Hopmans, J. W., 2008. On the value of soil moisture measurements in vadose zone hydrology: A review, *Water Resources Research*, **44**, W00D06.

Vogt, T., Hoehn, E., Schneider, P., and Cirpka, O. A., 2009. Untersuchung der Flusswasserinfiltration in voralpinen Schottern mittels Zeitreihenanalyse, *Grundwasser*, **14**, 179-194.

Vogt, T., Schneider, P., Hahn-Woernle, L., and Cirpka, O. A., 2010a. Estimation of seepage rates in a losing stream by means of fiber-optic high-resolution vertical temperature profiling, *Journal of Hydrology*, **380**, 154-164.

Vogt, T., Hoehn, E., Schneider, P., Freund, A., Schirmer, M., and Cirpka, O. A., 2010b. Fluctuations of electrical conductivity as a natural tracer for bank filtration in a losing stream, *Advances in Water Resources*, **33**, 1296-1308.

von Gunten, H. R., Karametaxas, G., and Keil, R., 1994. Chemical Processes in Infiltrated Riverbed Sediments, *Environmental Science & Technology*, **28**, 2087-2093.

von Gunten, U., and Zobrist, J., 1993. Biogeochemical changes in groundwater-infiltration systems - column studies, *Geochimica Et Cosmochimica Acta*, **57**, 3895-3906.

Vozoff, K., and Jupp, D. L. B., 1975. Joint inversion of geophysical data, *Geophysical Journal of the Royal Astronomical Society*, **42**, 977-991.

Ward, A. S., Gooseff, M. N., and Singha, K., 2010. Imaging hyporheic zone solute transport using electrical resistivity, *Hydrological Processes*, **24**, 948-953.

Ward, J. V., 1989. The four-dimensional nature of lotic ecosystems, *Journal of the North American Benthological Society*, **8**, 2-8.

Watanabe, T., Nihei, K. T., Nakagawa, S., and Myer, L. R., 2004. Viscoacoustic wave form inversion of transmission data for velocity and attenuation, *Journal of the Acoustical Society of America*, **115**, 3059-3067.

Waxman, M. H., and Smits, L. J. M., 1968. Electrical Conductivities in Oil-Bearing Shaly Sands, *Society of Petroleum Engineers Journal*, **8**, 107.

West, L. J., Handley, K., Huang, Y., and Pokar, M., 2003. Radar frequency dielectric dispersion in sandstone: Implications for determination of moisture and clay content, *Water Resources Research*, **39**, 1026.

Western, A. W., Grayson, R. B., and Blöschl, G., 2002. Scaling of soil moisture: A hydrologic perspective, *Annual Review of Earth and Planetary Sciences*, **30**, 149-180.

Wilkinson, P. B., Meldrum, P. I., Kuras, O., Chambers, J. E., Holyoake, S. J., and Ogilvy, R. D., 2010. High-resolution electrical resistivity tomography monitoring of a tracer test in a confined aquifer, *Journal of Applied Geophysics*, **70**, 268-276.

Winship, P., Binley, A., and Gomez, D., 2006. Flow and transport in the unsaturated Sherwood Sandstone: Characterization using cross-borehole geophysical methods, *Fluid Flow and Solute Movement in Sandstones: The Onshore UK Permo-Triassic Red Bed Sequence*, **263**, 219-231.

Wishart, D. N., Slater, L. D., and Gates, A. E., 2006. Self potential improves characterization of hydraulically-active fractures from azimuthal geoelectrical measurements, *Geophysical Research Letters*, **33**, L17314.

Woessner, W. W., 2000. Stream and fluvial plain ground water interactions: Rescaling hydrogeologic thought, *Ground Water*, **38**, 423-429.

Wombacher, A., and Schneider, P., 2010. Observation centric sensor data model, *Technical Report TR-CTIT-10-13, University of Twente, Enschede*, ISSN 1381-3625.

Woolsey, S., Capelli, F., Gonser, T., Hoehn, E., Hostmann, M., et al., 2007. A strategy to assess river restoration success, *Freshwater Biology*, **52**, 752-769.

Worthington, P. F., 1993. The uses and abuses of the archie equations 1. The formation factor porosity relationship, *Journal of Applied Geophysics*, **30**, 215-228.

Wriedt, G., and Rode, M., 2006. Modelling nitrate transport and turnover in a lowland catchment system, *Journal of Hydrology*, **328**, 157-176.

Wroblicky, G. J., Campana, M. E., Valett, H. M., and Dahm, C. N., 1998. Seasonal variation in surface-subsurface water exchange and lateral hyporheic area of two stream-aquifer systems, *Water Resources Research*, **34**, 317-328.

Yeh, T. C. J., Liu, S., Glass, R. J., Baker, K., Brainard, J. R., et al., 2002. A geostatistically based inverse model for electrical resistivity surveys and its applications to vadose zone hydrology, *Water Resources Research*, **38**, 1278.

Yeh, T. C. J., Lee, C. H., Hsu, K. C., Illman, W. A., Barrash, W., et al., 2008. A view toward the future of subsurface characterization: CAT scanning groundwater basins, *Water Resources Research*, **44**, W03301.

Yilmaz, Ö., 2001. *Seismic data processing*, Society of Exploration Geophysicists, Tulsa, USA.

Zhang, J., and Morgan, F. D., 1997. Joint Seismic and Electrical Tomography, *Proceedings of the Symposium on the Application of Geophysics to Engineering and Environmental Problems*, 391-396.

Zhdanov, M. S., 2009. New advances in regularized inversion of gravity and electromagnetic data, *Geophysical Prospecting*, **57**, 463-478.

Zhou, B., and Greenhalgh, S. A., 2003. Crosshole seismic inversion with normalized full-waveform amplitude data, *Geophysics*, **68**, 1320-1330.

Zonge, K., Wynn, J., and Urquhart, S., 2005. Resistivity, induced polarization, and complex resistivity, in *Near Surface Geophysics*, edited by D. K. Butler, pp. 265-300, SEG.

Zurbuchen, B. R., Zlotnik, V. A., and Butler, J. J., 2002. Dynamic interpretation of slug tests in highly permeable aquifers, *Water Resources Research*, **38**, 1025.